



# A Coronal Mass Ejection Source Region Catalog and Their Associated Properties

Satabdwa Majumdar<sup>1</sup> , Ritesh Patel<sup>1,2</sup> , Vaibhav Pant<sup>1</sup> , Dipankar Banerjee<sup>1,3,4</sup> , Aarushi Rawat<sup>5</sup>, Abhas Pradhan<sup>6</sup>, and Paritosh Singh<sup>7</sup>

<sup>1</sup> Aryabhatta Research Institute of Observational Sciences, Nainital, 263001, India

<sup>2</sup> Southwest Research Institute, 1050 Walnut Street, Suite 300, Boulder, CO 80302, USA

<sup>3</sup> Indian Institute of Astrophysics, 2nd Block, Koramangala, Bangalore, 560034, India

<sup>4</sup> Center of Excellence in Space Science, IISER Kolkata, Kolkata, 741246, India

<sup>5</sup> Department of Physics & Astrophysics, University of Delhi, Delhi, 110007, India

<sup>6</sup> Department of Physics, Indian Institute of Technology Kharagpur, Kharagpur, 721302, India

<sup>7</sup> UM-DAE Centre for Excellence in Basic Sciences, Mumbai, 400098, India

Received 2023 February 6; revised 2023 July 20; accepted 2023 July 23; published 2023 September 13

## Abstract

The primary objective of this study is to connect coronal mass ejections (CMEs) to their source regions, primarily to create a CME source region catalog, and secondarily to probe the influence that the source regions have on the different statistical properties of CMEs. We create a source region catalog for 3327 CMEs from 1998 to 2017, thus capturing the different phases of cycles 23 and 24. The identified source regions are segregated into three classes—active regions, prominence eruptions, and active prominences—while the CMEs are segregated into slow and fast groups, based on their average projected speeds. We find the contributions of these three source region types to the occurrences of slow and fast CMEs to be different in the above period. A study of the distribution of the average speeds reveals different power laws for CMEs originating from different sources, and the power laws are different during the different phases of cycles 23 and 24. A study of the statistical latitudinal deflections shows equatorward deflections, while the magnitudes of the deflections again bear imprints of the source regions. An east–west asymmetry is also noted, particularly in the rising phase of cycle 23, with the presence of active longitudes for the CMEs, with a preference toward the western part of the Sun. Our results show that different aspects of CME kinematics bear strong imprints of the source regions they originate from, thus indicating the existence of different ejection and/or propagation mechanisms of these CMEs.

Unified Astronomy Thesaurus concepts: Solar coronal mass ejections (310); Solar cycle (1487)

## 1. Introduction

Given the brisk advancements in science and technology, especially with our dependencies on space satellites and radio communications, a good understanding of space weather has become more of a necessity than a luxury. In this context, coronal mass ejections (CMEs) happen to be the major drivers of space weather and thus lie at the heart of our understanding of the same. These eruptions are capable of creating huge geomagnetic storms (Gosling 1993; Schwenn 2005). CMEs, in general, are defined as discrete, bright, white-light features that propagate outward in the coronagraph field of view (FOV) over timescales of few minutes to several hours (Hundhausen et al. 1984). This generic definition itself hints at the extent of the contrasts that are seen in the physical properties of CMEs, in terms of their masses, speeds, accelerations, widths, and energies (Webb & Howard 2012).

In order to study the behavior of CMEs, they are usually tracked in the corona on images taken by a coronagraph, the obvious reason behind such practice resting on the ability to create an artificial eclipse with the help of an occulting disk that blocks the disk of the Sun (Lyot 1930). Unfortunately, this creation of an artificial eclipse comes at the cost of obscuring the relevant disk features and a reasonable part of the inner corona (see Section 1 in Majumdar et al. 2020). This would make the observer sometimes incapable of distinguishing a

CME that originates around the disk center from a CME that originates at the limb (Majumdar et al. 2021b). As a consequence of this, primarily, a sense of the direction of propagation of the CME is lost and, secondarily, a rough estimate of the extent of the projection effect that would certainly creep into the measurements will also be lost (Balmaceda et al. 2018). Thus it seems obvious that white-light coronagraphic images are not enough for a holistic understanding of CME properties and propagation, and that it is equally important to locate and realize their source regions on the disk as well. This is also why extreme ultraviolet full-disk imagers are extremely important in the study of CMEs.

There have been several works identifying and associating CMEs with their source regions. Subramanian & Dere (2001) studied 32 CMEs from 1996 January to 1998 May, and they reported that 41% of the CMEs were from active regions (ARs), 15% were from quiescent prominences, while 44% of the CMEs were connected to prominence eruptions (PEs) that were connected to ARs. Zhou et al. (2003) studied 197 CMEs during the period from 1997 to 2001 and found that around 79% of the CMEs originated from ARs, while the rest originated from outside ARs. There have also been several other efforts at studying the locations of CME sources on the solar disk (Tripathi et al. 2004; Lara 2008; Yashiro & Gopalswamy 2009; Wang et al. 2011; Compagnino et al. 2017; Kim et al. 2017; Akiyama et al. 2019). Gao et al. (2014) reported that the association of solar surface activity with CMEs tended to vary during the rising and maximum phases of solar cycles 23 and 24. Moore et al. (2007) showed that the width of the CME can be used to estimate the strength of the



Original content from this work may be used under the terms of the [Creative Commons Attribution 4.0 licence](#). Any further distribution of this work must maintain attribution to the author(s) and the title of the work, journal citation and DOI.

magnetic field of the source region. Recently, Majumdar et al. (2021a) have showed that the source regions of CMEs have a clear imprint on the coupling of the CME kinematics happening at the inner and outer corona regions. It has also recently been shown by Pant et al. (2021) that the distributions of CME widths follow different power laws for CMEs originating from different source regions, and a similar imprint is also seen in the evolution of the 3D volume of CMEs (Majumdar et al. 2022). Thus, it seems there is a close relationship between CME properties and the source regions the CMEs originate from.

With regard to connecting the properties of CMEs to their source regions, catalogs connecting the same have proven very useful over the past few years. One of the most extensively used CME catalogs is the Coordinated Data Analysis Workshop (CDAW; Gopalswamy et al. 2009) catalog, which is a manual catalog that detects and records the different parameters of the CMEs in the LASCO FOV. There have also been some automated or semi-automated catalogs, like the Solar Eruptive Event Detection System (Olmedo et al. 2008), the Computer Aided CME Tracking (Robbrecht & Berghmans 2004; Pant et al. 2016), the Automatic Recognition of Transient Events and Marseille Inventory from Synoptic Maps (Boursier et al. 2009), and the Coronal Image Processing (Byrne et al. 2012; Morgan et al. 2012) catalogs. A dual-viewpoint CME catalog (JHUAPL; Vourlidas et al. 2017), on the other hand, relies on visual identifications of CMEs, while the measurements are taken through a semi-automated algorithm. Although the above catalogs provide comprehensive information about the CMEs that have been respectively detected, the one significant aspect that is missing from all of these catalogs is the information about the source regions of all the CMEs that have been cataloged.

In order to fill in this gap, we create a CME source region (CSR) catalog,<sup>8</sup> which is done by extracting CMEs (that occurred during the different phases of cycles 23 and 24) from the CDAW catalog. We also study the impressions of the identified source regions on the different statistical properties of CMEs, which will further signify the importance of a source region catalog for CMEs. In Section 2.1, we outline the different data sources that have been used in this work, followed by the working method that we have adopted. In Section 3, we present the results our work, and finally, in Section 4, we summarize the main conclusions of this work.

## 2. Data and Method

### 2.1. Data Source

We use the CDAW catalog to select and extract our events of interest. The source regions of the selected CMEs are identified by using data from the Extreme-Ultraviolet Imaging Telescope (Delaboudinière et al. 1995) on board the Solar and Heliospheric Observatory (SOHO; Domingo et al. 1995), the Atmospheric Imaging Assembly (AIA; Lemen et al. 2011) on board the Solar Dynamics Observatory (SDO), and the two coronagraphs, COR-1 and COR-2, and the Extreme Ultraviolet Imager (Wuelser et al. 2004) of the Sun Earth Connection Coronal and Heliospheric Investigation (SECCHI; Howard et al. 2008) on board the Solar Terrestrial Relations

**Table 1**  
The Number of CMEs Studied in This Work, During the Different Phases of Cycles 23 and 24

Solar Cycle	Cycle Phase	Year	No. of Events
Cycle 23	Rising	1998	171
Cycle 23	Rising	1999	174
Cycle 23	Maxima	2000	289
Cycle 23	Maxima	2001	132
Cycle 23	Maxima	2002	71
Cycle 23	Declining	2003	57
Cycle 23	Declining	2004	218
Cycle 23	Declining	2005	87
Cycle 23	Minima	2008	78
Cycle 23	Minima	2009	113
Cycle 24	Rising	2010	158
Cycle 24	Rising	2011	269
Cycle 24	Rising	2012	382
Cycle 24	Maxima	2013	860
Cycle 24	Maxima	2014	23
Cycle 24	Declining	2017	245

Observatory (STEREO; Kaiser et al. 2008); refer to Section 2.4 for details on the source region identification.

### 2.2. Event Selection

The CMEs for this work were selected from the CDAW catalog in such a way that different phases of solar cycle 23 and 24 could be considered. Thus, we selected CMEs that occurred from 1998 January to 2017 December. This allowed us to capture the rising phases, the maxima, and the declining phases of the cycles (Table 1). First, the “very poor” CMEs, as quoted in the CDAW catalog, are removed from our sample, as Wang & Colaninno (2014) reported that the detection of these “very poor” CMEs was based on the discretion of manual operators. Further, the source region identification and the derived kinematics of these “very poor” CMEs are ambiguous. Thus, in order to remove such untoward bias and any discrepancies that might intrude into our analysis, we discard them. Next, during the pre-STEREO era, on-disk observations of the backside of the Sun with respect to the Sun–Earth line were not available. This led to the removal of all those CMEs for which no source region could be identified on the frontside of the Sun, as, for such cases, the source regions were located behind the limb. Further, after the launch of STEREO, there were certain source regions that were located in unobserved regions combining the STEREO and SOHO viewpoints, and thus it was not possible to identify their source regions either. During the period considered in this work, there were also certain cases of the unavailability of data from the disk imaging instruments (mentioned in Section 2.1), which further restricted the number of events.

### 2.3. Classification of Slow and Fast CMEs

The CMEs thus selected for study are classified into slow and fast, based on the average (linear) speed as provided in the CDAW catalog. In this regard, the CDAW catalog quotes the average speed at which the leading edge of the CME travels in the FOV of the coronagraphs. This classification is done based

<sup>8</sup> <https://allssc.aries.res.in/catalogs>

on the speed of the CME relative to the ambient solar wind speed. It is known that the slow solar wind usually travels with speeds of less than around  $400 \text{ km s}^{-1}$ , and on the other hand, the fast solar wind shows evidence of speeds higher than  $400 \text{ km s}^{-1}$ , as reported by Schwenn (2006). Thus, for a statistical study, the average solar wind speed can be considered to be around  $400 \text{ km s}^{-1}$ . Based on this average solar wind speed, we tag CMEs with speeds higher than  $500 \text{ km s}^{-1}$  as fast CMEs and the ones with speeds less than  $300 \text{ km s}^{-1}$  as slow CMEs (see Pant et al. 2021). Further, since we are considering projected speeds for this classification, the CMEs with speeds ranging between  $300$  and  $500 \text{ km s}^{-1}$  can strictly be considered neither as fast nor slow. This is due to the uncertainties in the projected speeds, and thus they are classified as intermediate CMEs. In this context, it should also be noted that since we are working with projected speeds, the results of this work will be suffering from projection effects, as the true speeds for the CMEs originating from the disk center will be different than their projected speeds.

#### 2.4. Identification and Classification of Source Regions of CMEs

To identify and associate (spatially and temporally) the source regions of the CMEs, we follow a similar procedure as reported in Subramanian & Dere (2001), Majumdar et al. (2020), and Pant et al. (2021), and we use the JHelioviewer software (Muller et al. 2009; Müller et al. 2017) to backproject the CMEs onto the solar disk. In order to do this, we consider a spatial and temporal window of criteria in order to associate a CME to its source region. For a spatial association between a source region and a CME originating from it, we require the latitude of the source region to be within around  $\pm 30^\circ$  of that of the position angle (PA) of the center of the CME, as reported in the CDAW catalog (see Gilbert et al. 2000; Majumdar et al. 2020; Pant et al. 2021). When the spatial extent of the source region is large, the latitudes and longitudes of the boundaries are recorded and their mean is computed. For a temporal association, an eruption or radially outward motion is considered in the abovementioned window of latitude, within a minimum time of 30 minutes before the CME leading front is first observed in the LASCO C2 FOV. However, it must also be kept in mind that this temporal criterion was kept flexible and was decided based on the quoted speed of the CME in the CDAW catalog. The different disk imaging and coronagraph data, as mentioned in Section 2.1, are loaded into the JHelioviewer software to create base difference movies that can help in connecting the outgoing CMEs to the source region on the disk.

After identifying the source regions by the above procedure, the identified source regions are then broadly classified into three categories: (a) ARs; (b) PEs; and (c) active prominences (APs; see Majumdar et al. 2020; Pant et al. 2021). The ARs are regions of predominantly strong magnetic fields, which are much denser and hotter compared to the background plasma of the corona, producing bright emission in the extreme ultraviolet and soft X-ray wavelengths (Figure 1(a)). A prominence, on the other hand, is cool dense material ( $8000 \text{ K}$ ) that is embedded in the relatively hotter corona, which is identified as an emission feature when it is observed at the solar limb (Figure 1(b)) and identified as a dark absorption feature when it is seen on the disk, projected against the background hotter corona (called filament; Gilbert et al. 2000). A source region is

considered to be a PE if a strong radial motion is identified away from the surface of the Sun, where all or some part of the prominence material is observed to escape the Sun's gravitational field. For a filament eruption (which is included in the same category as PEs in this work), either a tangential motion across the Sun's surface was noted, followed by a subsequent eruption, or simply any disappearance of a pre-existing filament was noted, which was then followed by a transient coronal manifestation (also refer to Webb & Hundhausen 1987). Thus, it should be noted that PEs correspond to erupting prominences located in quiet-Sun regions (outside ARs). The third category, APs, considers PE events where the prominence (with one or more of its footpoints) is embedded in an AR (Figure 1(c); see Subramanian & Dere 2001).

### 3. Results

#### 3.1. Overall Statistics

In Figure 2(a), we show the overall fractional occurrences of the slow, fast, and intermediate CMEs during our studied period. We find that  $\sim 43\%$  of the studied CMEs were slow CMEs, while  $\sim 24\%$  of the CMEs were fast CMEs and  $\sim 33\%$  were intermediate CMEs. Thus, we see that the majority of our studied CMEs were slow CMEs. In Figure 2(b), we show the overall contributions of the three different source regions that we have considered in this work. We find that ARs contribute to  $\sim 65\%$  of the studied CMEs, APs contribute to  $\sim 12\%$  of the studied CMEs, and  $\sim 23\%$  of the total CMEs come from PEs. Thus, we find that although most of the CMEs are originating from ARs, there are also a considerable number of CMEs originating from PEs, which are located in the quiet-Sun regions.

#### 3.2. Yearly Occurrence

In Figure 3(a), we plot the yearly occurrences of slow and fast CMEs during our period of study. The color-coded histograms denote the occurrences of slow and fast CMEs relative to each other for each year. On the right-hand side, we have plotted another y-axis, which displays the relative percentage of occurrences of slow and fast CMEs with respect to the total CMEs, for ease of appreciating the differences. In Figure 3(a), the squares represent the relative occurrences of slow CMEs and the circles represent the relative occurrences of fast CMEs, while in Figure 3(b), the squares represent the relative contributions of ARs, the circles are for APs, and the triangles are for PEs. Please note that since the intermediate CMEs cannot strictly be considered as either fast or slow CMEs, and since, in this work, we are more interested in the slow and fast CMEs, we will not be including the intermediate CMEs in the analysis. In Table 1, we have grouped the yearly studied CMEs into different subclasses, according to the phase of the solar cycle that the considered years correspond to (see Hathaway 2015; Jha et al. 2022). It should be noted here that we tried to be unbiased with the selection and hence the contribution of any particular category of CMEs under consideration, by studying CMEs that occurred during different phases of cycles 23 and 24. Moreover, since this work relies on statistical analysis, the conclusions arrived at from the overall behavior of a sample will not change. Based on that, we find that during the rising phase, and as the cycle progresses toward the maximum, for both cycles 23 and 24, the fractional occurrences of slow CMEs start decreasing, and, on the other

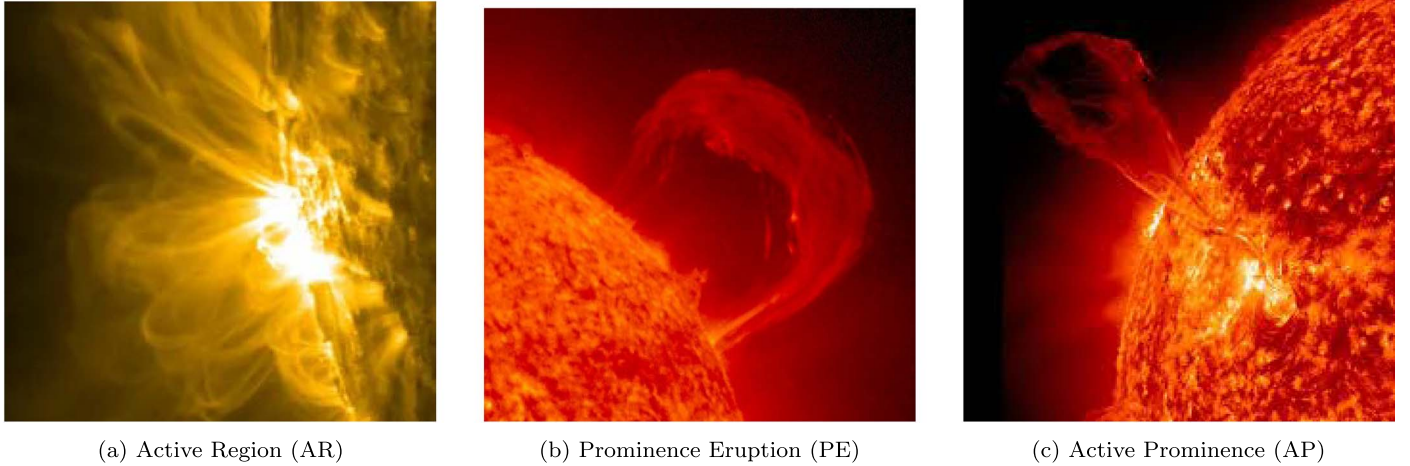


**Figure 1.** This figure shows examples of the three source region categories that have been considered in this work. (a) An AR is shown, which is exhibiting bright emission in AIA 171 Å. (b) A PE is shown, which is located at the quiet-Sun region, in AIA 304 Å. (c) An AP is shown in AIA 304 Å, where we can see that the footpoint of the prominence is connected to an AR.

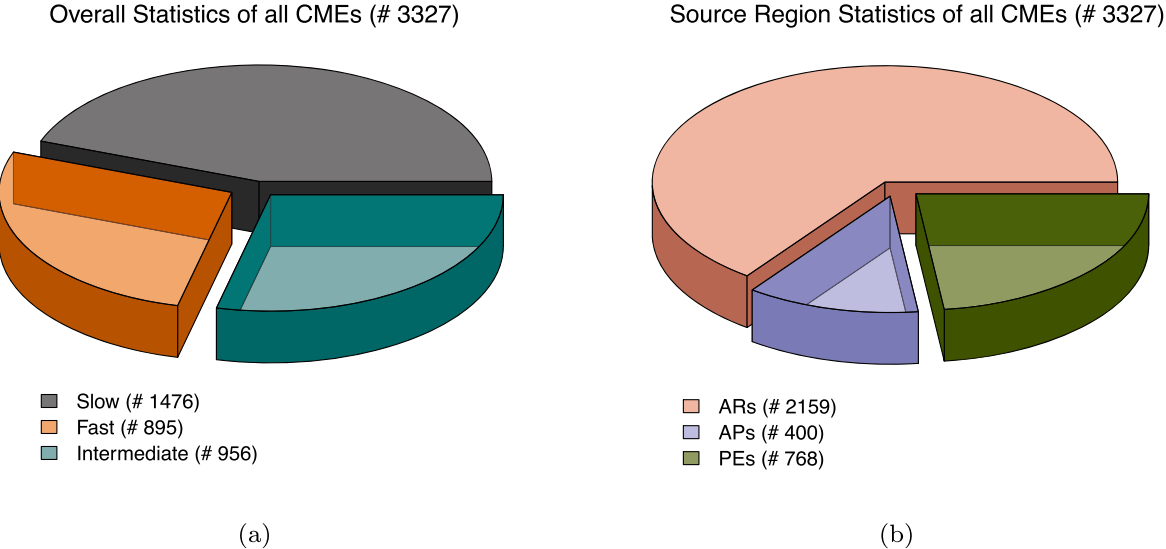


**Figure 2.** Fractional occurrences of (a) slow, fast, and intermediate CMEs and (b) the fractional contributions of the different source regions to the CMEs during the studied period.

hand, the fractional occurrences of fast CMEs start increasing. As a result, during the solar maximum, we find almost similar occurrences of slow and fast CMEs. It is also important to note here that despite considering similar numbers of months in the maxima phases of cycles 23 and 24, the number of CMEs (slow and fast) as shown in the histograms is higher in the cycle 24 maxima as compared to the cycle 23 maxima, thus confirming the occurrence of more CMEs in a similar period of study in cycle 24 than 23. This is supported by the report on the relatively higher CME rate in cycle 24 compared to cycle 23 by Lamy et al. (2019), where Gopalswamy et al. (2014) suggested a weakening of the overall poloidal field that led the weaker CMEs to escape out into the heliosphere. This is further reflected in the fact that the number of slow CMEs in cycle 24 always exceeds the number of fast CMEs (Figure 3(a)). The declining phase, on the other hand, shows a swinging/alternating behavior, indicating repeating increases and/or decreases in the fractional occurrences of the slow and fast CMEs. However, as the cycle further progresses toward the minimum, we see that the fractional occurrences of slow CMEs

largely exceed the occurrences of fast CMEs. We also see that even for solar minimum, we do not get to see many fast CMEs, but we do get to observe a reasonable number of slow CMEs. Thus, during the solar minimum, while the Sun is expected to remain quiet, in terms of CMEs, the Sun is not really quiet.

Since it is evident that the occurrences of slow and fast CMEs vary during the different phases of a solar cycle, it also becomes imperative to look into the origins of such variations. In order to do that, we first plot in Figure 3(b) the yearly contributions of the different source region types (which are, in our work, ARs, APs, and PEs) to the CMEs (both slow and fast). We find that the contributions of the ARs dominate over the contributions from APs and PEs for most phases of the solar cycle. However, during the solar minimum of cycle 23, we find that the contributions of the ARs drop down, which is expected, but at the same time, the contributions of the PEs rise up. Thus we see that during the minimum phase, most of the CMEs are coming from the PEs, which are rooted into the quiet-Sun region. The contribution of APs is found to be comparatively less than those from ARs and PEs. As the cycle

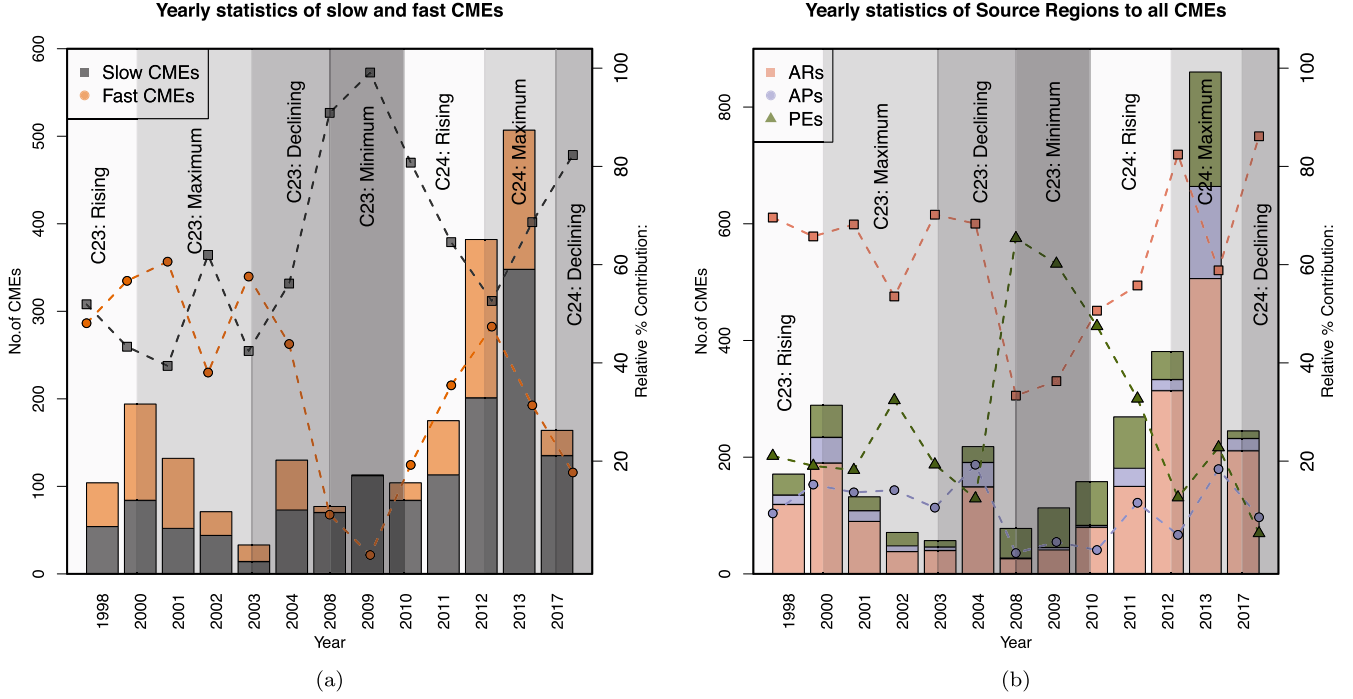


**Figure 3.** This figure shows the yearly occurrences of (a) slow and fast CMEs, and (b) the contributions of different source regions to the CMEs. The histograms are color-coded according to the categories they are representing. The y-axis on the left-hand side denotes the number of events that the histograms are representing. We also show the relative contribution of each category in each year (with respect to the total number of events in that particular year) on the y-axis plotted on the right-hand side, corresponding to the data points connected by dotted lines. The different phases of the solar cycle are highlighted in the background in different gray-scale shades.

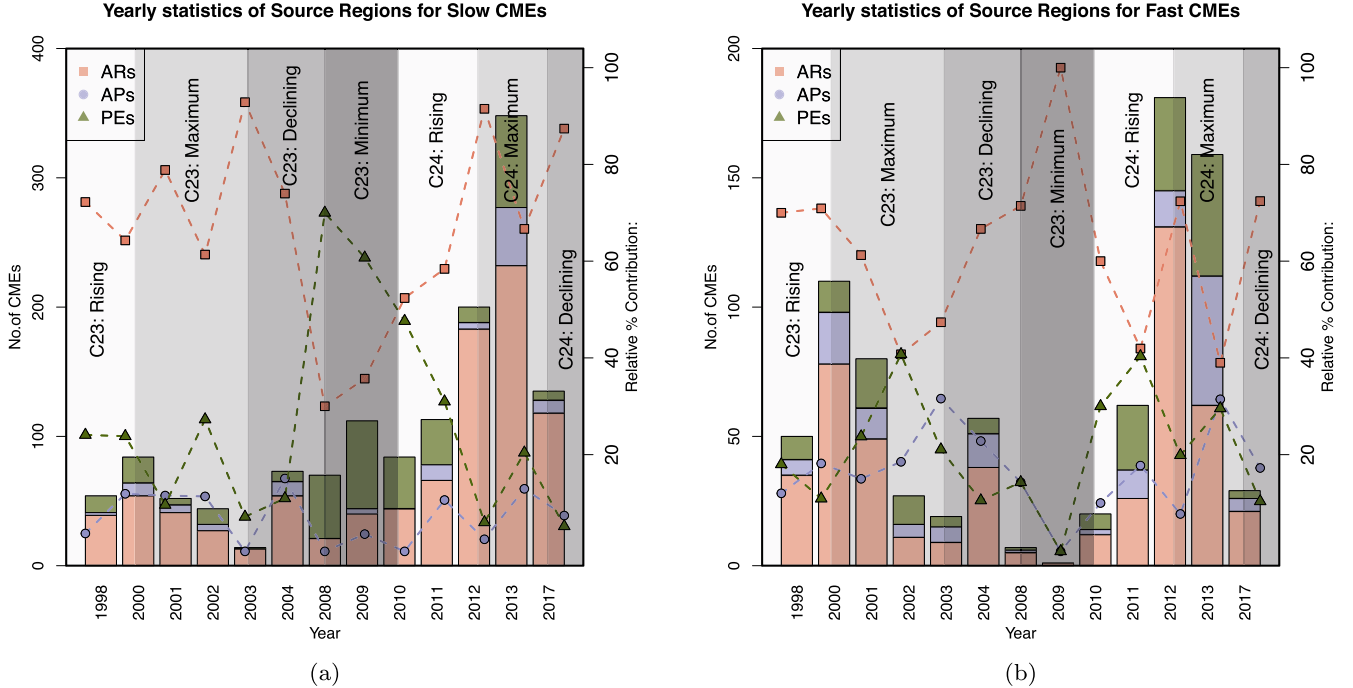


**Figure 4.** Yearly contributions of the source regions to (a) slow CMEs and (b) fast CMEs. The histograms are color-coded according to the category they are representing. The y-axis on the left-hand side denotes the number of events that the histograms are representing. We also show the relative contribution of each category in each year (with respect to the total number of events in that particular year) on the y-axis plotted on the right-hand side, corresponding to the data points connected by dotted lines. The different phases of the solar cycle are highlighted in the background in different gray-scale shades.

progresses toward the solar maximum, we can see that the number of contributions from the PEs increases, but the contribution from the ARs during the same period increases even more, and hence leads to a declining trend of the relative contribution from the PEs.

Having found that apart from the variations in the slow and fast CMEs across the different phases of the solar cycle, the contributions of the different source regions also vary, it becomes crucial to combine these two results and thereby find the essence of the variations in slow and fast CMEs coming

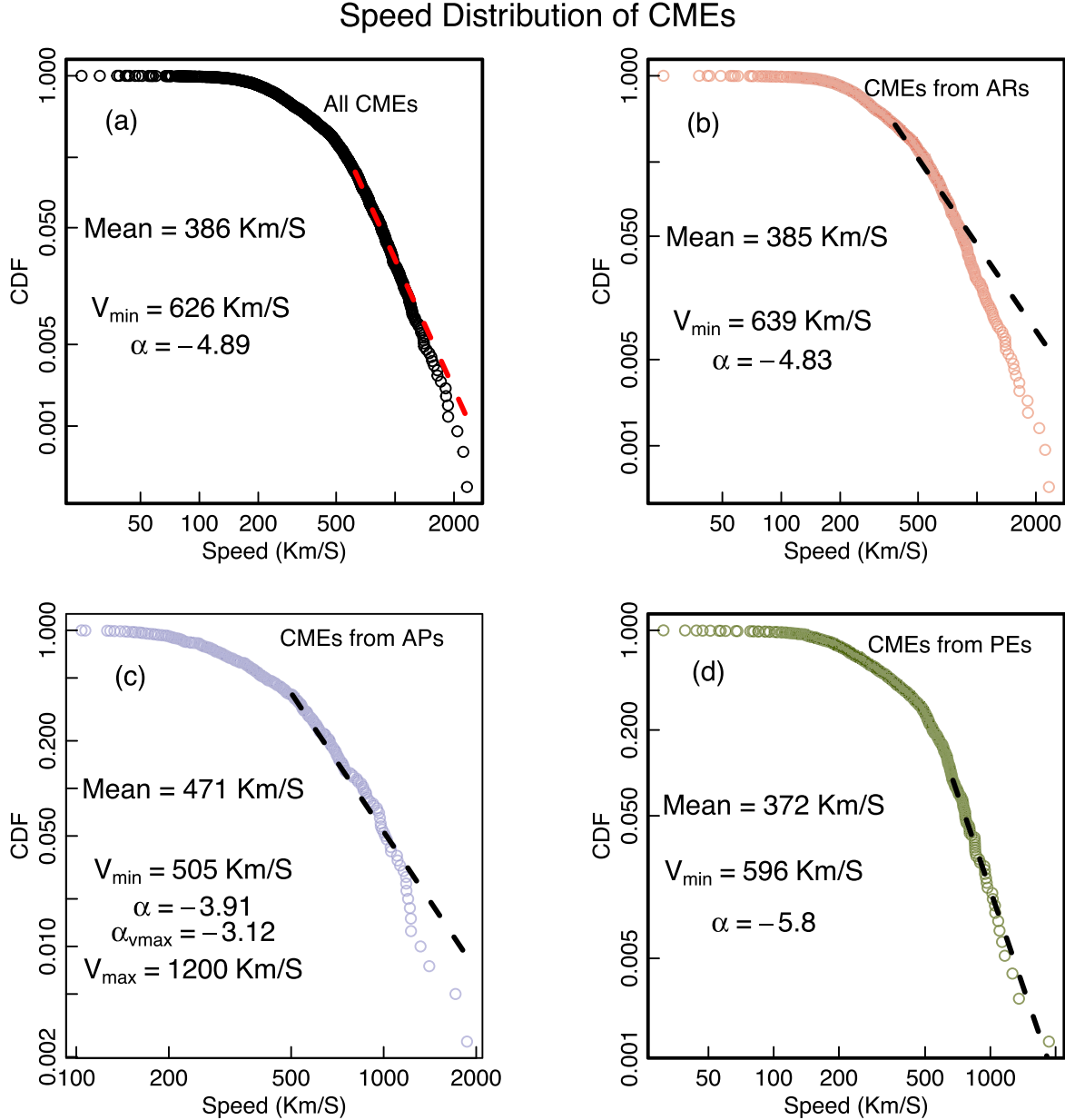


**Figure 5.** In this figure, we plot (d) the distribution of the average speed of all CMEs and the distributions of the average speeds of CMEs coming from ARs, APs, and PEs in (b), (c), and (d) respectively. A power law is fitted to the data based on the MLE technique (dashed line). The power-law index ( $\alpha$ ) and the mean speed are also provided in each panel.

from these different source regions. To do that, in Figure 4, we look into the contributions of these source regions to slow CMEs (in panel (a)) and fast CMEs (in panel (b)) separately. In the case of slow CMEs (Figure 4(a)), we see that the contribution of ARs increases as the cycle progresses from the rising phase to the cycle maximum in both cycles 23 and 24. During the minimum in cycle 23, we see that the contribution of the ARs drops down, while the contribution from the PEs increases. Thus we note that most of the slow CMEs occurring during the solar minimum in cycle 23 arise from PEs. In this context, Lugaz et al. (2017) have reported that these slow CMEs are often capable of driving shocks and hence they are of importance from the space weather perspective as well. Thus, it is important to capture and understand the variations of these slow CMEs, whose occurrences exceed the occurrences of fast CMEs during the solar minimum. As the

cycle progresses further, from the minimum of cycle 23 to the rising phase and then the maximum of cycle 24, we again see that the contributions of ARs increase much more than the contributions from PEs, and once again the contributions from APs are found to be much less than the contributions from the other two classes. However, it is also worth noting that separating the APs from the other two classes has facilitated the demarcation of the contributions from the ARs and the PEs during the different phases of the solar cycle.

In the case of the fast CMEs (Figure 4(b)), the contribution of the ARs is higher than the ones from the APs and PEs. Nevertheless, we also find that the contribution of the APs to fast CMEs is much higher than its contribution to slow CMEs. The contribution of PEs also increases as the cycle progresses from the rising phase to the maximum phase, while during the minimum, in cycle 23, we find that the handful of fast CMEs

**Table 2**  
The Fitted Power-law Indices for the CMEs Coming from Different Source Regions During Different Phases of Cycles 23 and 24

Average Speed for	$v_{\min}$	Power-law Index ( $\alpha$ )	$v_{\max}$	$\alpha$ with $v_{\max}$	$P$ -value
All CMEs	626	-4.89	...	...	0.72
CMEs from ARs	639	-4.83	...	...	0.96
CMEs from APs	505	-3.91	1200	-3.12	0.75
CMEs from PEs	596	-5.80	...	...	0.66
All CMEs (C23—Rising)	401	-3.48	1000	-2.48	0.88
All CMEs (C24—Rising)	576	-4.87	1600	-5.07	0.94
All CMEs (C23—Maximum)	602	-4.57	1600	-4.20	0.87
All CMEs (C24—Maximum)	478	-4.74	1000	-3.81	0.65
All CMEs (C23—Declining)	555	-4.28	...	...	0.86
All CMEs (C24—Declining)	450	-5.84	900	-6.97	0.91
All CMEs (C23—Minimum)	190	-4.06	650	-5.17	0.94
CMEs from ARs (C23—Rising)	400	-3.32	1000	-2.86	0.45
CMEs from ARs (C24—Rising)	651	-5.25	1500	-5.04	0.76
CMEs from APs (C23—Rising)	487	-4.04	950	-3.84	0.90
CMEs from APs (C24—Rising)	545	-4.03	1300	-3.59	0.96
CMEs from PEs (C23—Rising)	445	-3.98	1600	-4.32	0.48
CMEs from PEs (C24—Rising)	596	-5.68	1100	-6.46	0.59
CMEs from ARs (C23—Maximum)	585	-4.59	1500	-4.17	0.88
CMEs from ARs (C24—Maximum)	447	-4.93	900	-3.31	0.49
CMEs from APs (C23—Maximum)	655	-5.03	1200	-3.98	0.87
CMEs from APs (C24—Maximum)	675	-5.32	1900	-4.80	0.87
CMEs from PEs (C23—Maximum)	653	-6.24	1000	-6.85	0.98
CMEs from PEs (C24—Maximum)	586	-5.04	...	...	0.64
CMEs from ARs (C23—Declining)	563	-4.28	1500	-4.52	0.41
CMEs from ARs (C24—Declining)	444	-5.35	950	-5.55	0.70
CMEs from APs (C23—Declining)	401	-3.61	...	-	0.64
CMEs from APs (C24—Declining)	254	-3.05	950	-3.19	0.64
CMEs from PEs (C23—Declining)	273	-3.03	700	-2.51	0.31
CMEs from PEs (C24—Declining)	137	-2.18	800	-1.61	0.08
CMEs from ARs (C23—Minimum)	157	-3.24	500	-4.39	0.61
CMEs from APs (C23—Minimum)	...	...	...	...	...
CMEs from PEs (C23—Minimum)	203	-5.99	800	-6.66	0.92

**Note.** The minimum cutoff ( $v_{\min}$ ) for the fitted power law is tabulated in the second column. A second power-law index ( $\alpha$  with  $v_{\max}$ ) is also provided in the fifth column for the upper cutoff ( $v_{\max}$ , which is given in the fourth column) at the tail of the distribution. The associated  $p$ -values for the fitted power laws are provided in the final column.

that occur mostly originate from ARs. Interestingly, we also note that the contribution of the APs exceeds the contribution from the PEs during the declining phases of cycles 23 and 24.

### 3.3. Distribution of Average CME Speeds

The average speeds have been extracted from the CDAW catalog, which are the projected speeds. In Figure 5, we plot the distribution of the average CME speeds. We plot the cumulative distribution function here, as it is straightforward to calculate, and no binning is required, which further removes the bias that is often introduced by the choice of bin widths (White et al. 2008). In panel (a), we plot the distribution of the average speeds of all the CMEs, where the mean speed of the distribution is  $386 \text{ km s}^{-1}$ , and to that we fit a power law. In order to get a better estimate on the fitted power law to a discrete data set (see D’Huys et al. 2016), we use the Maximum Likelihood Estimate (MLE) technique to fit the power law. From Figure 5, a minimum value of the speed (say,  $v_{\min}$ ) is seen (for which the power-law behavior is observed), and the choice of this  $v_{\min}$  parameter is crucial as it in turn dictates the power-law index. Thus, to find  $v_{\min}$ , first an initial guess of  $v_{\min}$

is set as the minimum value of the data set. Now, for a given  $v_{\min}$ , the MLE technique is used to fit a power law to the data. Then the entire data set is scanned with different values of  $v_{\min}$ , and finally  $v_{\min}$  is decided for which the Kolmogorov–Smirnov (K-S) distance (Clauset et al. 2009) for the fitted power law is minimized. Recently, Majumdar et al. (2020) reported that the cataloged speeds, especially for fast CMEs, can be highly misleading, as they are often observed as halo or partial-halo CMEs, and for such CMEs, there can be a reasonable overestimation of their propagation speeds, and the cataloged speeds can also be mistaken for their expansion speeds. Further, these CMEs are less frequent and tend to occur in clusters (Ruzmaikin et al. 2011), seldom exhibiting extreme kinematic properties (Gopalswamy et al. 2018). As a result, the tail of the distribution often shows a sudden break, where the power-law behavior is no longer followed. Thus, to remove the influence of the data points occurring at this broken tail, we put an upper cutoff ( $v_{\max}$ ) to the fitted power law, indicating that any data above  $v_{\max}$  are to be ignored for fitting. In Table 2, we have listed the power-law indices for all the categories discussed above, the lower cutoff  $v_{\min}$ , the upper cutoff  $v_{\max}$ , their corresponding power-law indices, and the associated  $p$ -

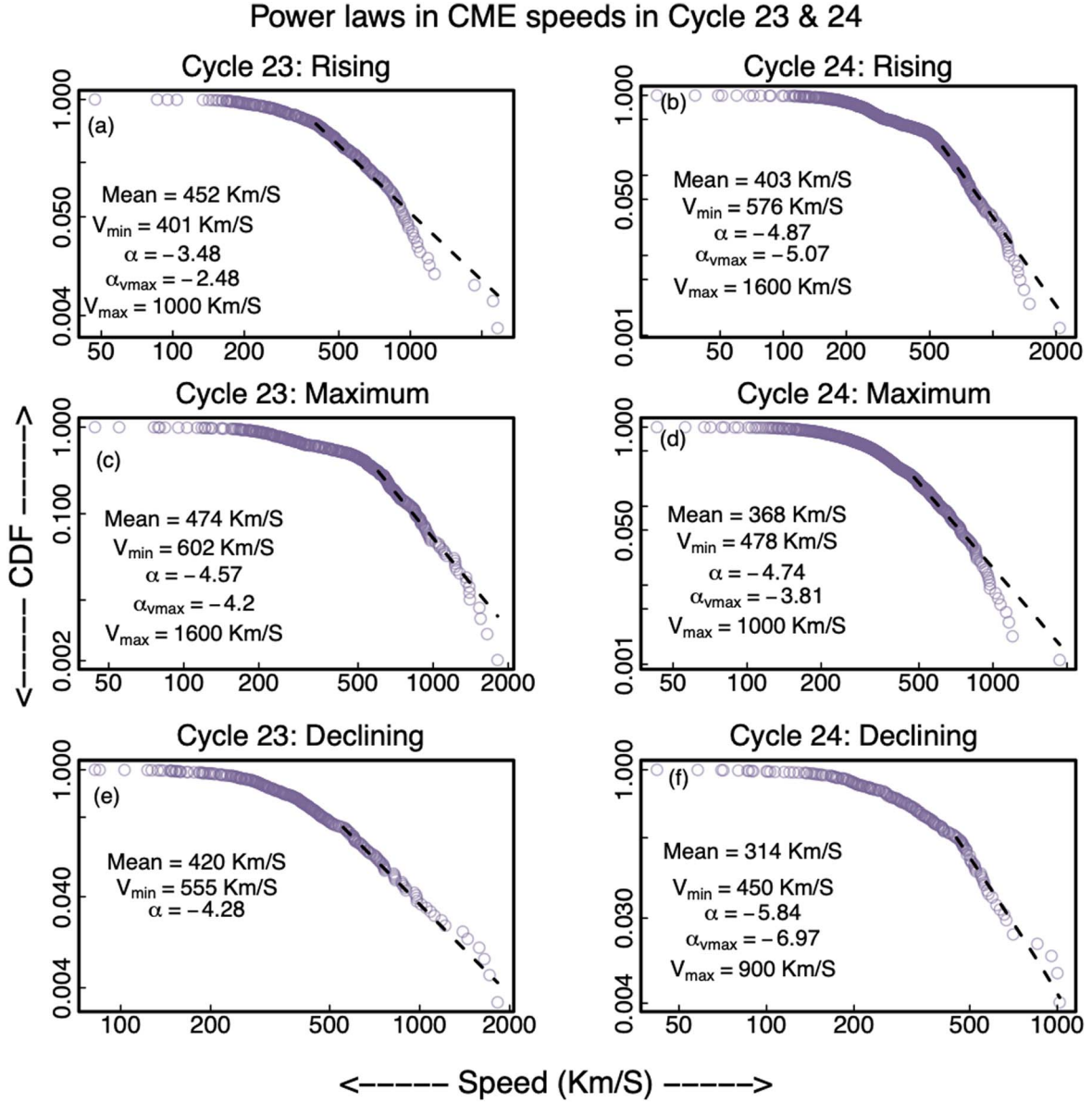


**Figure 6.** This figure shows the speed distributions of the CMEs, fitted with power laws (dashed lines), for different phases of the solar cycles 23 and 24. The fitted power-law index ( $\alpha$ ) is mentioned in each case.

values for the statistical significance of the fitted power laws. It can be seen that the  $p$ -values are higher than the threshold value (0.05), thus indicating their statistical significance. Please note that the upper cutoff  $v_{\max}$  and the corresponding  $\alpha$  are provided for only those cases for which a break in the tail of the distribution is noted. We find a power law index of  $-4.89$ . Since we have the information about the source regions the CMEs are coming from, in panels (b), (c), and (d) we again fit power laws separately for the CMEs originating from ARs, APs, and PEs, using the same technique. In this case, we find average speeds of  $385 \text{ km s}^{-1}$ ,  $471 \text{ km s}^{-1}$ , and  $372 \text{ km s}^{-1}$  for the distributions of speeds of the CMEs from ARs, APs, and PEs, respectively. We find that the average speed of the CMEs from APs is higher than the average speed for the CMEs from ARs. This is due to the fact that the number of slow CMEs largely exceeds the number of fast CMEs in cycle 24 (see Figure 3), and in Figure 4, we see that most of these slow CMEs are contributed from the ARs. Further, Gopalswamy

et al. (2020) reported the average lower potential energy of the ARs, which has resulted in a larger number of weak and slow CMEs in cycle 24. We find that CMEs originating from different source regions follow different power-law profiles. The CMEs originating from PEs follow a steeper power law, with a power-law index of  $-5.8$ , than the ones originating from ARs and APs, which have power-law indices of  $-4.83$  and  $-3.91$ , respectively. Here, in the case of the CMEs coming from APs, we note a break in the tail of the distribution, and thus by implementing the  $v_{\max}$  parameter, we find a slight change in the power-law index, with the new  $\alpha$  being  $-3.12$ . Pant et al. (2021) have recently shown that the power laws associated with the widths of slow and fast CMEs also show a similar trend, with the width of the CMEs originating from PEs following a steeper power law than the ones from ARs. It seems that the width and speed distributions of CMEs tend to exhibit similar imprints of the source regions on them.

### 3.4. Variation of Speed Distribution with the Phase of Solar Cycle

In Figure 6, we plot the distributions of the average speeds of CMEs, occurring during similar phases of cycle 23 and 24, adjacent to each other. In panels (a) and (b), we plot the distributions of the speeds during the rising phases of cycles 23 and 24. We find that the mean speed is higher in cycle 23 ( $467 \text{ km s}^{-1}$ ) as compared to cycle 24 ( $405 \text{ km s}^{-1}$ ) for the rising phase. For the maximum phase, in panels (c) and (d), we again get a similar trend. The average speed in the cycle 23 maximum is  $484 \text{ km s}^{-1}$ , while that in the cycle 24 maximum is much lower, with a mean speed of  $370 \text{ km s}^{-1}$ . For the decaying phase, again we find that the mean speed is higher in cycle 23 ( $434 \text{ km s}^{-1}$ ) as compared to the mean speed in cycle 24 ( $314 \text{ km s}^{-1}$ ). Thus, overall, we find that the average speeds during cycle 24 are always less than the average speeds in cycle 23, irrespective of the phase of the solar cycle considered (see Gopalswamy et al. 2014). Apart from that, another observable trend is that in cycle 23, the average speed is highest in the maxima, followed by the rising phase, and then the minima, with the lowest average speed, while such a trend is not seen in cycle 24. In cycle 24, we find that the average speed is highest in the rising phase, followed by the rising phase, with the minimum average speed in the declining phase. We now fit a power-law distribution to the data as well. For the rising phase, we find a power-law index of  $-3.48$  for cycle 23 and  $-4.87$  for cycle 24. For the maximum phase, we find a power-law index of  $-4.37$  for cycle 23 and  $-4.74$  for cycle 24, while for the declining phase, a power-law index of  $-4.28$  is found for cycle 23 and a power-law index of  $-5.84$  is found for cycle 24. Thus, we find that the speed distribution follows different power laws during different phases of the solar cycle. In cycle 23, we find that the maximum phase has the steepest power law, followed by the declining phase, with a much less steep power law in the rising phase. However, this is not the case for cycle 24, where we find the declining phase to have the steepest power law, followed by the rising phase, and then the maximum phase. From Figure 6, a break in the tail of the distribution is noted in almost all the cases, and hence a power law is also fitted by including the upper cutoff  $v_{\max}$ . However, we find here that this trend remains unchanged with the inclusion of  $v_{\max}$  for the fitting, although it must also be noted that the difference in the power-law index for the rising phase and the maximum phase is much less compared to the differences with the other power-law indices. Apart from that, we also see that the distributions of average speeds follow a much steeper power law for cycle 24, as compared to cycle 23, and this behavior is independent of the phase of the solar cycle being considered.

It has now become clear that the speed distributions of CMEs follow different power laws in different phases of cycles 23 and 24. Since we have the extra information about the source regions of these CMEs, it is also worth looking at the imprints of these source regions on these particular variations of the power laws in the speed distributions across the different phases of cycles 23 and 24. In Figure 7, we plot the speed distributions of the CMEs originating from ARs, APs, and PEs and occurring during the rising phases of cycles 23 and 24. In the left panels of the plot, we include the CMEs occurring in cycle 23, and in the right panels, we include the ones occurring in cycle 24. In cycle 23, we find power-law indices of  $-3.32$ ,  $-4.04$ , and  $-3.98$  for the CMEs originating from ARs, APs, and PEs, respectively. Thus, we see in the cycle 23 rising

phase, that the CMEs coming from APs tend follow the steepest power law, followed by the CMEs from PEs and then those from ARs. On the other hand, in cycle 24, we find the CMEs coming from PEs to have the steepest power laws, followed by the CMEs coming from APs, and then the ones from ARs. Thus, in cycle 24, we find that the CMEs coming from PEs follow a steeper power law than the ones originating from ARs. This is also in agreement with the results of Pant et al. (2021), who reported a steeper power law in the width distribution of the CMEs from PEs compared to the CMEs from ARs.

Similarly, in Figure 8, we plot the speed distributions of the CMEs originating from ARs, APs, and PEs and occurring during the maximum phases of cycles 23 and 24. In this case, for cycle 23 (in the left panels), we again find that the CMEs coming from PEs have a much steeper power law of  $-6.24$ , followed by a power law of  $-5.03$  for the CMEs from APs, and then a power law of  $-4.34$  for the ones from ARs. For cycle 24, we find a similar trend, with the steepest power law being followed by the CMEs from PEs, with a power-law index of  $-5.04$ , followed by the CMEs from APs, with a power law of  $-5.01$ , and  $-4.93$  for the CMEs from ARs. Thus, the CMEs from PEs follow a much steeper power law compared to the CMEs from ARs and APs, irrespective of the solar cycle under consideration. For the cases in which a break in the tail of the distribution is observed, we again fit a power law by including  $v_{\max}$  in the fitting process, and we find that, in some cases, there is an appreciable change in the power law, but the trend of the power laws remains unchanged.

In Figure 9, we similarly plot the speed distributions for the declining phases of cycles 23 and 24. Contrastingly, we find that in cycle 23, the CMEs coming from ARs follow the steepest power law, with a power-law index of  $-4.28$ , followed by the CMEs from APs, with a power law of  $-3.61$ , and then the CMEs from PEs, with a power law of  $-3.03$ . A similar trend is also followed in cycle 24 as well. We find the steepest power law of  $-5.35$  to be followed by the CMEs from ARs, followed by  $-3.05$  for the CMEs from APs, and then the CMEs from PEs, with a power law of  $-2.18$ . Although it should be noted here that the numbers of events in the classes of APs and PEs in cycle 24 are less than the number of events in the class of ARs, and the smaller number of data points may affect the derived power laws, as reported by D’Huys et al. (2016). Having said that, it is surprising that the trend of the imprint of the source regions on the distribution of the speeds reverses in the declining phase of the solar cycle, when compared to the trends set up in the rising and maximum phases. However, it must also be noted that the numbers of data points for the cases of CMEs from PEs and APs are much less compared to the number of data points for the CMEs from ARs (see Figure 3(b)), and hence in the future, the inclusion of more events for CMEs from PEs and APs will be important for understanding the trend that is followed in the declining phase of the solar cycle.

We study the distribution of the average speeds in the minimum phase of cycle 23 in Figure 10. In panel (a), we plot the distribution for all the CMEs (from the different source regions) and fit a power law to it. We find a power-law index of  $-4.06$ , which is less than what we found for the maximum phase of cycle 23 (Figure 6). In panels (b), (c), and (d), we plot the same for the CMEs from ARs, APs, and PEs, respectively. Since the number of events in the category of APs (in panel (c))

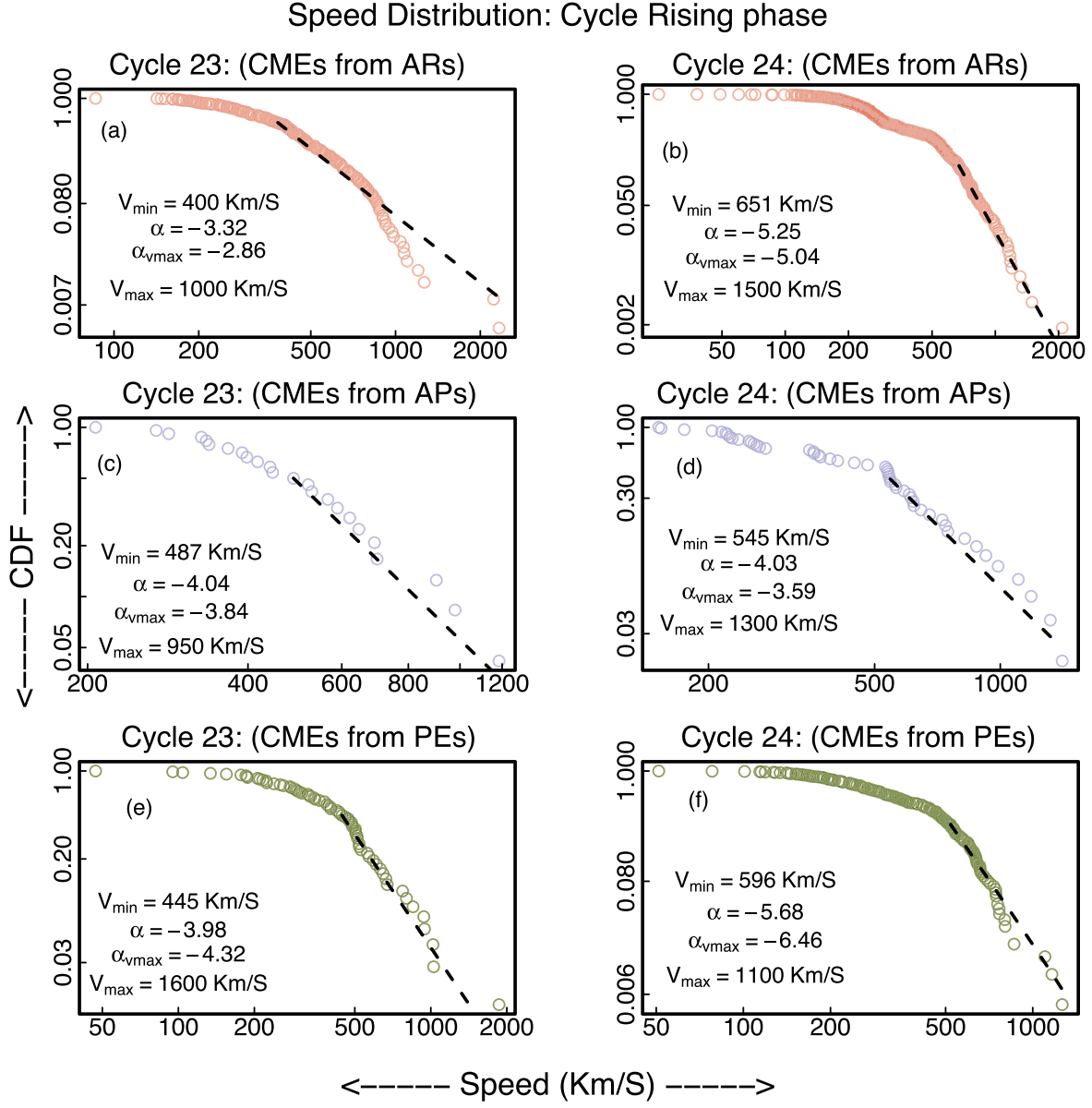


**Figure 7.** This figure shows the variation of the speed distributions of the CMEs originating from the three different source regions (ARs, APs, and PEs) and occurring during the rising phases of cycles 23 and 24. A power law is also fitted to the data (dashed line) and the power-law index ( $\alpha$ ) is mentioned in each case.

is very small, we were not able to fit a power law to it. We find a power law of  $-3.24$  for CMEs originating from ARs and a power law of  $-5.99$  for CMEs coming from PEs. Thus, in the case of the minimum phase of cycle 23, we also see the CMEs from PEs follow a steeper power law in their speed distributions, with respect to the other categories. Thus, it seems the mechanisms responsible for the CMEs attaining average speeds might be different for CMEs from PEs compared to the ones connected to ARs, and this is independent of the phase of the solar cycle. In this case, too, we notice a break in the tail of the distributions in (a) and (b), and after including  $v_{\max}$  for the fitting, we see that the trends of the power laws remain unchanged.

### 3.5. Latitudinal Deflections of CMEs

A study of the deflections of CMEs forms an integral part of the understanding of the spatial relationship between CMEs and their source regions. In this work, we investigate the

occurrences of latitudinal deflections in the CMEs considered here. In order to do that, we first convert the central position angle (CPA) of the CME to its corresponding equivalent latitude (with the assumption that the event is happening at the plane of the sky). This implies that a CME with a CPA of  $90^\circ$  will have an equivalent latitude of  $0^\circ$ , and the same will also hold for a CME with a CPA of  $270^\circ$ . In this context, it should be kept in mind that the CPA is measured on the plane of the sky and hence suffers from projection effects, which may lead to a conversion redundancy in the estimated latitudes, as this conversion assumes the strict radial propagation of CMEs, which is not always the case. Thus, in the future, working with the actual latitudes of the CMEs found from 3D reconstructions will be crucial. A CME with a CPA of  $155^\circ$  will correspond to a latitude of  $-65^\circ$ , which is  $65^\circ$  south, while a CME with a CPA of  $295^\circ$  will have an equivalent latitude of  $25^\circ$  north. This conversion from the CPA to the equivalent latitude can be

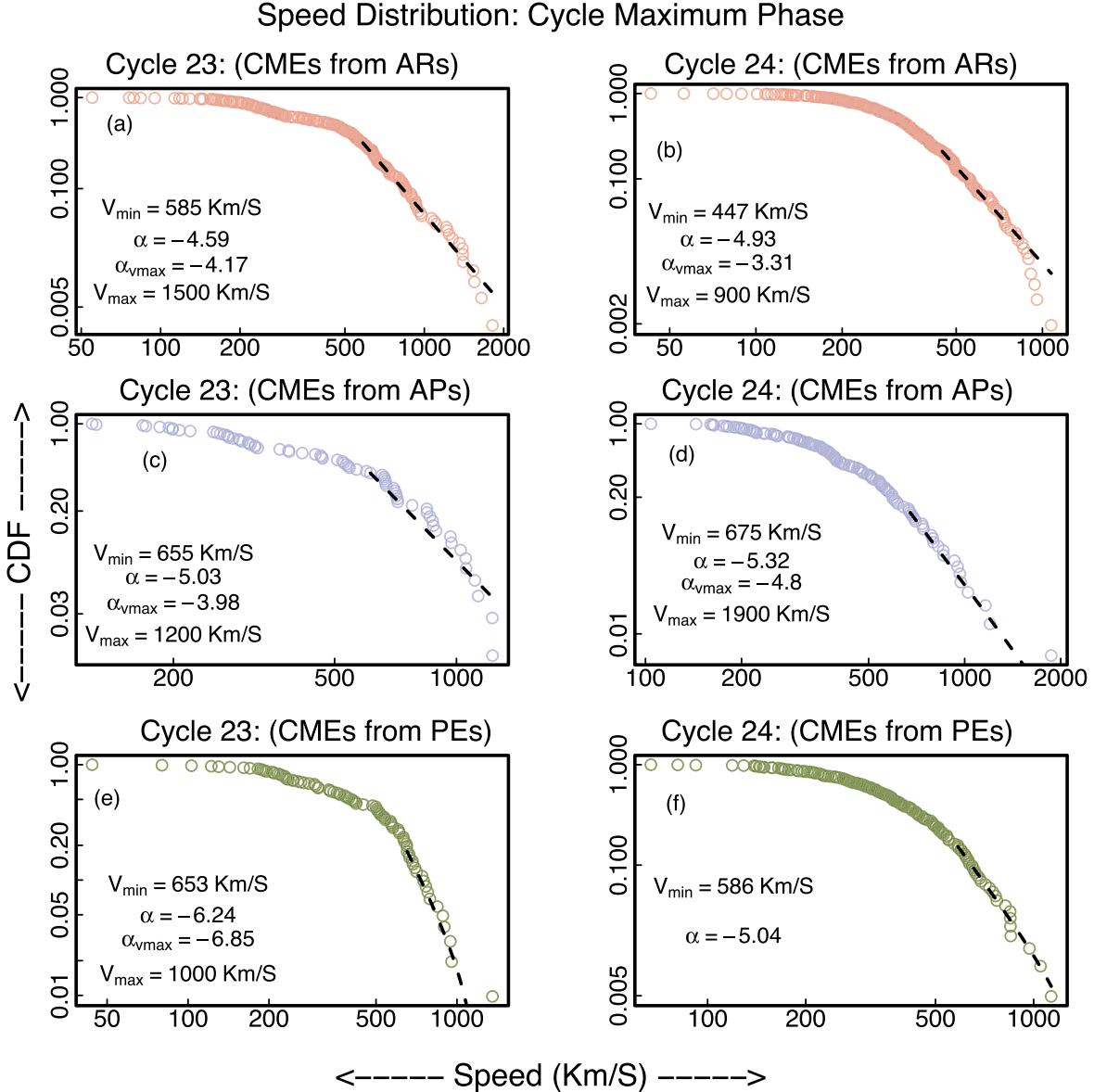


**Figure 8.** This figure shows the variation of the speed distributions of the CMEs originating from the three different source regions (ARs, APs, and PEs) and occurring during the maximum phases of cycles 23 and 24. A power law is also fitted to the data (dashed line) and the power-law index ( $\alpha$ ) is mentioned in each case.

generalized into the following:

$$\begin{aligned} \text{lat}_{\text{PA}} &= 90 - \text{CPA} \quad [0 \leq \text{CPA} \leq 180] \\ \text{lat}_{\text{PA}} &= \text{CPA} - 270 \quad [180 < \text{CPA} \leq 360], \end{aligned} \quad (1)$$

where  $\text{lat}_{\text{PA}}$  is the equivalent latitude corresponding to the CPA. However, it should be noted here that  $\text{lat}_{\text{PA}}$  is a projected quantity and thus, in the future, for more precise estimations of deflections, the deflection magnitude can be estimated from the actual 3D parameters (see Majumdar et al. 2020).

In Figure 11(a), we plot the distribution of the latitudes of the source regions of all the CMEs in the top part, followed by the distribution of the  $\text{lat}_{\text{PA}}$  for all the CMEs in the bottom part. In the top part, we find a bimodal distribution, with the peaks of the distribution lying at the active latitudes, around  $\pm 10^\circ$ – $20^\circ$ , although we also notice contributions from higher latitudes as well. In the distribution of  $\text{lat}_{\text{PA}}$ , however, we do not find a similar bimodal distribution: we notice a single peak centered around the zero value, which is the equator, indicating that

most of the CMEs, after being ejected at their respective source locations, were deflected toward the equator. A similar trend has also been reported in earlier works (see Gopalswamy et al. 2003; Cremades & Bothmer 2004; Gui et al. 2011; Wang et al. 2011), based on the association between source regions and CMEs. In our case, too, since we have the source region information, we similarly plot the distributions of the latitudes of the source regions, the equivalent latitudes of the CMEs, and the differences between the two latitudes, separately, for CMEs coming from ARs, APs, and PEs in panels (b), (c), and (d). We find that for all three categories, the distributions of the latitudes of the source regions are once again double-peaked. While the distributions for ARs and APs peak around  $10^\circ$ – $20^\circ$ , the distribution for PEs peaks around  $20^\circ$ – $30^\circ$ . Further, the distribution for PEs is more widely spread out, to almost all latitudes, as was also reported in Gopalswamy et al. (2003), while the distribution for CMEs from APs resembles that of ARs, ranging between  $\pm 40^\circ$ . We also see that the distribution of  $\text{lat}_{\text{PA}}$  for PEs is more spread out than is the case for ARs and

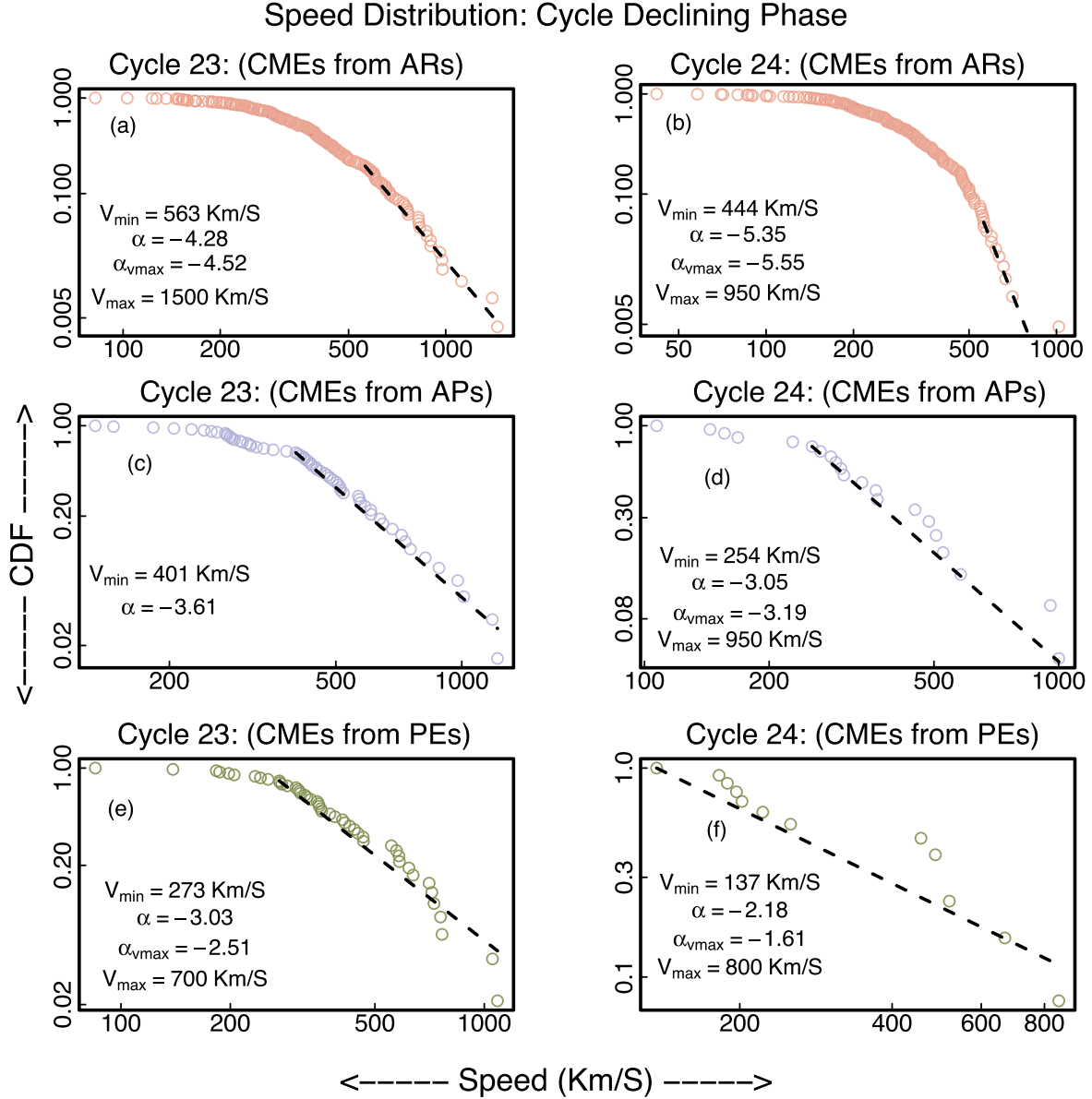


**Figure 9.** This figure shows the variation of the speed distributions of the CMEs originating from the three different source regions (ARs, APs, and PEs) and occurring during the declining phases of cycles 23 and 24. A power law is also fitted to the data (dashed line) and the power-law index ( $\alpha$ ) is mentioned in each case.

APs, thus indicating that the deflections, which are predominantly equatorial for the CMEs originating from ARs or APs, are not so for the CMEs coming from PEs. This behavior might be an outcome of the fact that a reasonable fraction of PEs are located at higher latitudes.

To understand the magnitude of the deflection suffered by the CMEs, we plot in Figure 12 the distribution of the difference of the above two latitudes in each case. We find that the distribution is centered around the zero value, indicating that most of the CMEs suffered a small magnitude of deflections. This is true for the cases of CMEs originating from ARs, APs, and PEs, as well. To have a better quantification of the same, in Figure 12, we again plot the distribution of the difference between the source region latitudes and the CPA equivalent latitudes of the CMEs, fitting a Gaussian to the distribution. The mean and the standard deviation of the fitted Gaussian are also shown. Further, since the deflection magnitude calculated in this way can be either

positive or negative, the mean of the deflection magnitude might be misleading, and hence we also quote the mean of the absolute deflection magnitudes ( $\mu_a$ ). In panels (b), (c), and (d), we separately consider CMEs coming from ARs, APs, and PEs, respectively. We find that the CMEs coming from PEs have the lowest mean and absolute mean deflection magnitudes, of  $0.8^\circ$  and  $18.2^\circ$ , while the CMEs from APs have mean and absolute mean deflection magnitudes of  $-2.5^\circ$  and  $20.1^\circ$ , respectively, and those from ARs have  $-2.1^\circ$  and  $20.4^\circ$ . The standard deviations are similar for ARs and APs ( $26.9^\circ$  and  $26.7^\circ$ , respectively), while it is comparatively less for CMEs from PEs ( $23.9^\circ$ ). Thus, it seems that although CMEs from PEs exhibit signatures of deflections both toward and away from the equator (as found in Figure 11(d)), the magnitudes of the deflections are not as spread out as in the cases for CMEs connected to ARs or APs.

In Figure 13, we study the distributions of the magnitudes of latitudinal deflection occurring during the different phases of

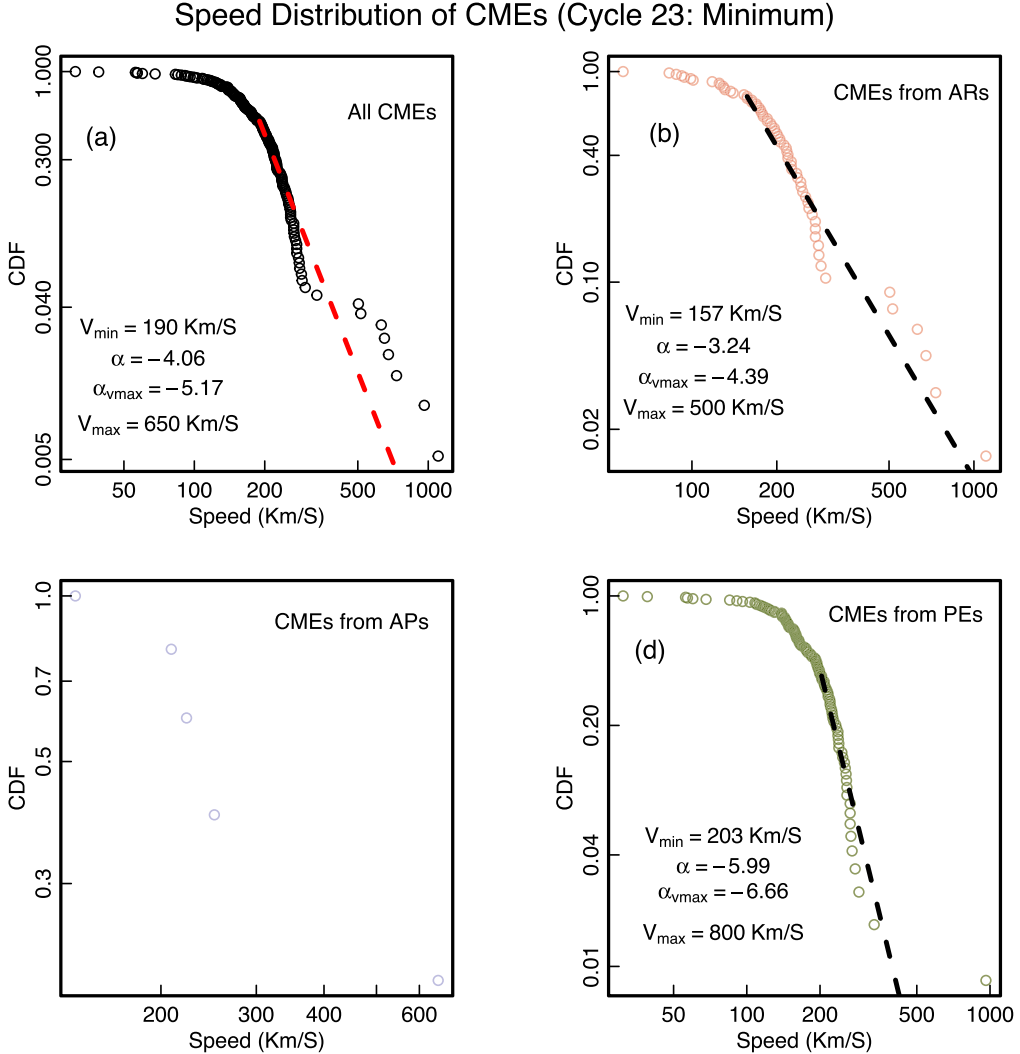


**Figure 10.** This figure shows the variation of the speed distributions of all CMEs in panel (a), and those originating from the three different source regions (ARs, APs, and PEs) in panels (b), (c), and (d), respectively, during the minimum phase of cycle 23. A power law is also fitted to the data (dashed line) and the power-law index ( $\alpha$ ) is mentioned in each case.

cycle 23, as well as studying if there is any imprint of the source region category on the variation of these distributions. Plotted along the horizontal rows are the distributions for the rising phase, the maximum phase, and the declining phase, for each of the three source region categories. Plotted in each vertical column are the variations of the distributions with source region category for each of the three phases of cycle 23. We find that for CMEs connected to ARs or APs, the standard deviation is at its lowest during the rising phase (20.4 for ARs and 14.7 for APs), it is relatively higher in the maximum phase (26.8 for ARs and 21.8 for APs), and it is the highest during the declining phase, with values of 31° and 26.7 for ARs and APs, respectively. For PEs, too, we see a similar trend, with a standard deviation of 17.5 in the rising phase, one of 22.1 in the maximum, and a similar standard deviation in the declining phase (21.6) as that during the maximum phase. The standard deviations we find in this work are slightly higher than the overall standard deviation reported by Yashiro & Gopalswamy (2009), although they include only flaring regions under the consideration of the source regions, while not considering the phase of the solar cycle under consideration, as is done in this work. This is due to the fact that Yashiro & Gopalswamy

(2009) included only those CMEs for which the longitudes of the associated flares were confined between 45° and 85°, while we do not put any such constraint on our events. This is reflected in a relatively lesser spread in the difference of the PA distributions.

To understand the variation of the deflection magnitude in cycle 24, we plot a similar set of figures for cycle 24 in Figure 14. In this case, we find that for CMEs coming from ARs and APs, the standard deviation is highest in the maximum phase (31.8 for ARs and 25.6 for APs), as compared to the rising phase (26.4 for ARs and 20.8 for APs), thereby reaching the minimum standard deviations in the declining phase (17.3 and 15.3 for the CMEs from ARs and APs, respectively). Although we see a similar trend in case of PEs as well (21.5 in the rising phase and 24.6 in the maximum phase), the standard deviation is higher in the decaying phase, but it should also be noted that the number events in the declining phase for PEs is also much less. Thus, it is evident that the statistical deflection trends are different during the different phases of the solar cycle, and they are also dependent on the solar cycle under consideration.

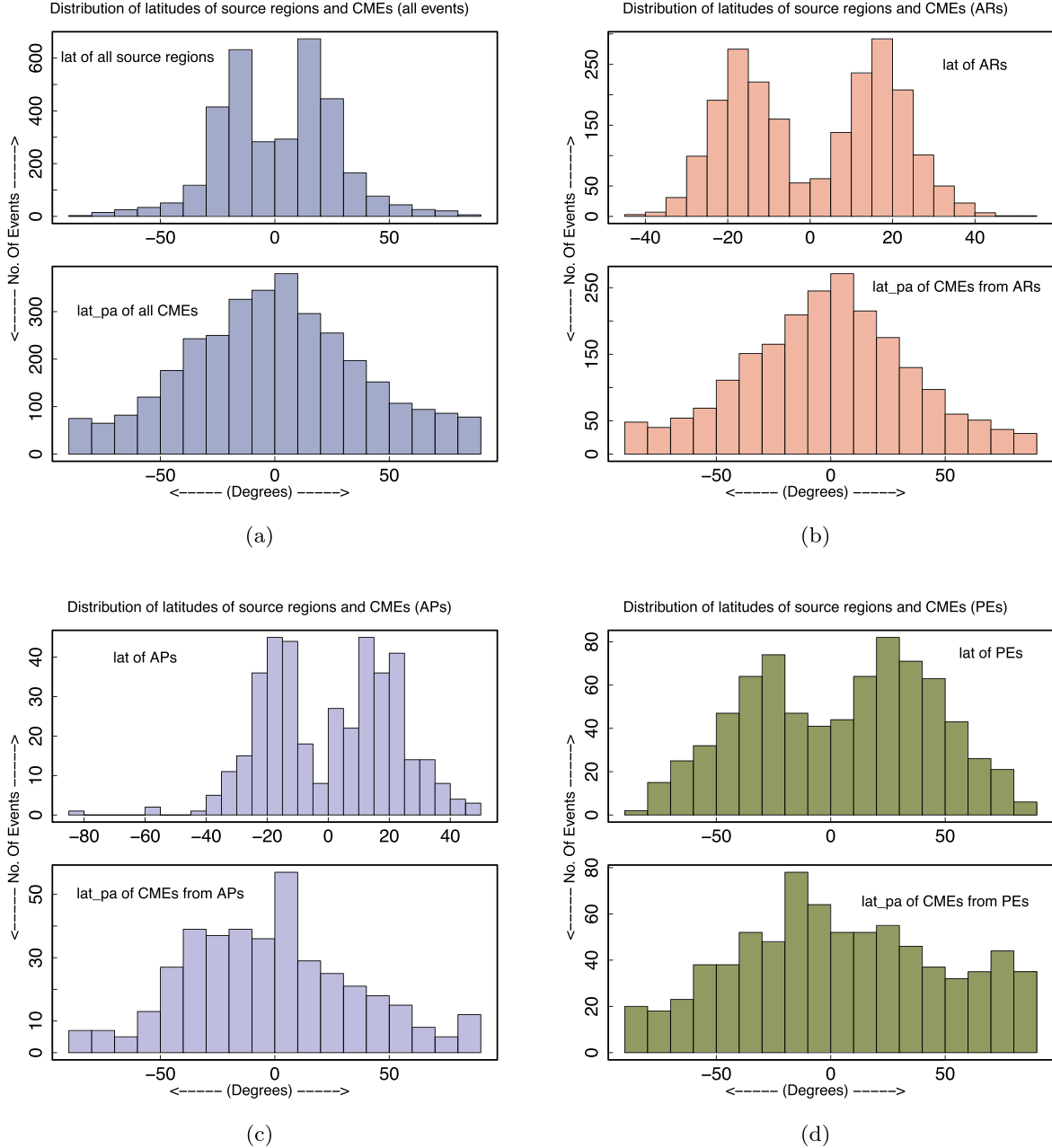


**Figure 11.** Latitudinal deflections of CMEs are plotted for all the CMEs in panel (a) and for the CMEs coming from ARs, APs, and PEs in panels (b), (c), and (d), respectively. In each panel, the top part shows the distribution of the latitude of the source region, with a double-peak signature in all four cases. Distributions of the position-angle equivalent latitudes are plotted in the bottom parts.

To understand the nature of the deflections in the minimum phase, we plot the distributions of the deflection magnitudes for the CMEs occurring during the minimum phase of cycle 23 in Figure 15. We get an overall standard deviation of  $22.5^\circ$  for all the CMEs (in panel (a)). What is worth noting in this case are the standard deviations for the CMEs coming from ARs and PEs (in panels (b) and (d)), since, for the want of statistics, we could not fit a Gaussian for the CMEs coming from APs (in panel (c)). For the case of ARs, the standard deviation is  $17.4^\circ$ , while for the CMEs coming from PEs, the standard deviation is  $25.1^\circ$ . Thus, we see that unlike in the rising phase, the maximum phase, or the declining phase (as shown in Figures 13 and 14), in the minimum phase of cycle 23, the standard deviation of the deflection magnitude is relatively higher for CMEs coming from PEs compared to ARs. In the

future, it will be worth noting if such a trend is also observed in the minimum phase of cycle 24 as well. In Table 3, we have listed the mean deflections, the mean of the absolute deflections, and the standard deviations for all of the categories discussed above.

### 3.6. Distributions of Longitudes of Source Regions

After studying the latitudinal deflections, we study the distributions of the longitudes of the source regions in Figure 16. In panel (a), we plot the distribution of the longitudes for all CMEs, and in panels (b), (c), and (d), we plot the same for the CMEs coming from ARs, APs, and PEs, respectively. In each plot, we also shade the region that highlights the significance of the contribution of the STEREO

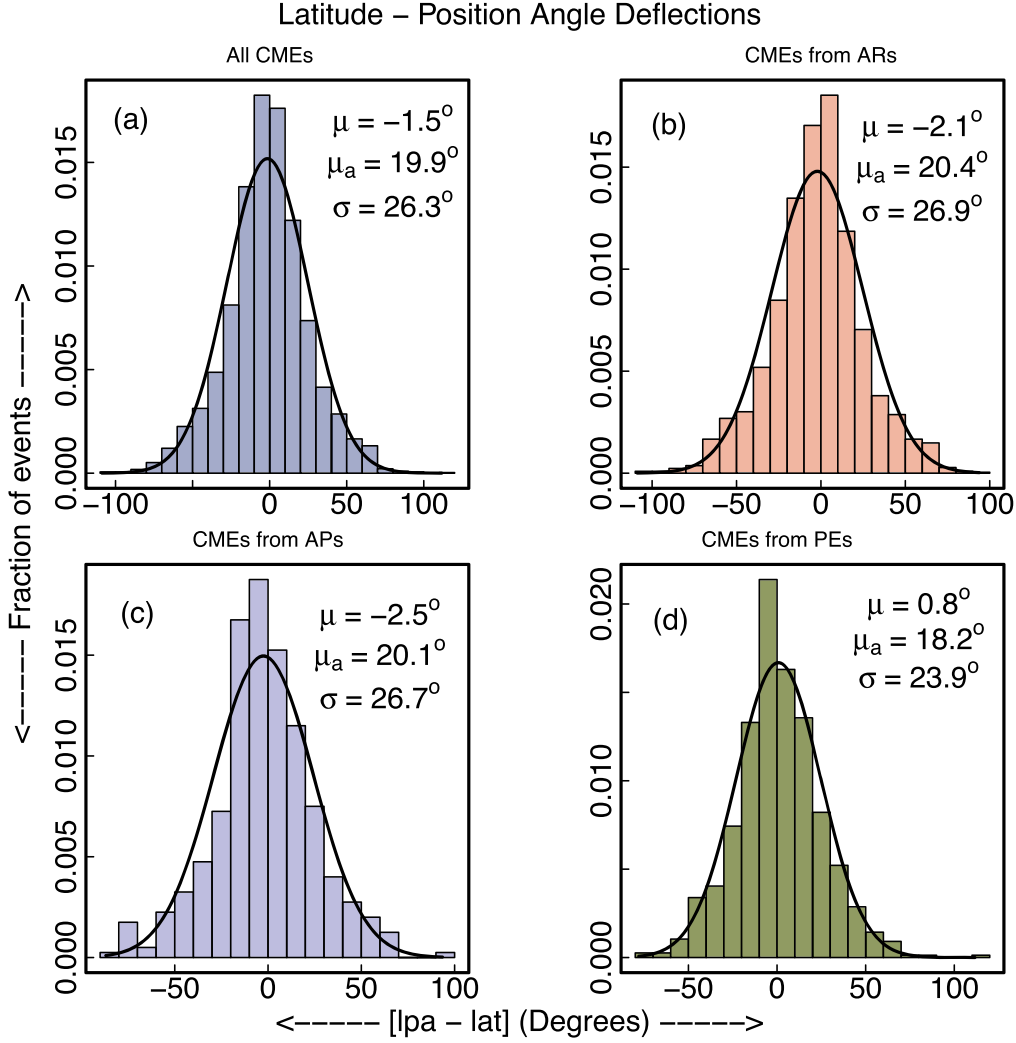


**Figure 12.** The distribution of the difference between the latitudes of the source regions of the CMEs and the position-angle equivalent latitudes of the CMEs is plotted for all CMEs in panel (a) and for CMEs originating from ARs, APs, and PEs in panels (b), (c), and (d), respectively. A Gaussian is also fitted to all four cases and the mean ( $\mu$ ), the absolute mean ( $\mu_a$ ), and the standard deviation ( $\sigma$ ) for each of the fitted Gaussians are also shown in each plot.

mission in helping us to locate and identify the source regions that were located at the backside of the Sun, with respect to the Sun–Earth line. Please note that a longitude of  $0^\circ$  denotes the central meridian with respect to Earth. Thus, longitudes lying between  $90^\circ$  and  $180^\circ$  signify the backside of the western limb, while longitudes lying between  $-90^\circ$  and  $-180^\circ$  signify the backside of the eastern limb. We find a clear double-peak signature of the longitude distribution for all four cases (where we find that the peaks of the distributions tend to lie in the range  $\pm 40^\circ$ – $100^\circ$ ). This indicates a relatively higher contribution of CMEs originating close to the solar limb. The CMEs that originate around the central meridian are generally less prone to being detected, owing to projection effects. Further, the events studied in this catalog are selected from the CDAW catalog, which records CMEs detected along the Sun–Earth line. Observations from STEREO that facilitated quadrature observations only started after 2009, so it could be possible that the relative abundance of CMEs from the limb region might be an outcome of their detection happening only along the Sun–Earth line. We also find that there is a predominant east–west asymmetry in the distribution of the source region longitudes, with a higher contribution coming from the western half of the Sun.

Skirgiello (2005) reported on the existence of this east–west asymmetry in CMEs by studying the CMEs that occurred during 1996–2004, but their conclusions were inferred from the asymmetry in the position angles of the CMEs, instead of the actual source longitudes. In order to check for the same, in Figure 17, we plot the distributions of the position angles of the CMEs. It should be noted that in terms of the position angles, the position angles lying between  $0^\circ$  and  $180^\circ$  denote CMEs along the eastern limb, while the ones with position angles between  $180^\circ$  and  $360^\circ$  denote CMEs at the western limb. We see that, in this case, we do not get to see any asymmetry in the two peaks of the distribution, while it is only for the case of the CMEs coming from APs that we do see a clear east–west asymmetry, with a dominance coming from the eastern hemisphere (which is also opposite to what we observe in Figure 16(c)). Further, using the position angles to infer the longitudinal asymmetry has its own limitations, as discussed by the authors themselves in Skirgiello (2005). Thus, studying the distribution of position angles can be misleading in this context, and so working with the actual longitudes of the source locations is encouraged.

To check whether this asymmetry undergoes any change during the different phases of cycles 23 and 24, as considered

## Latitude – Position Angle Deflections (Cycle 23)

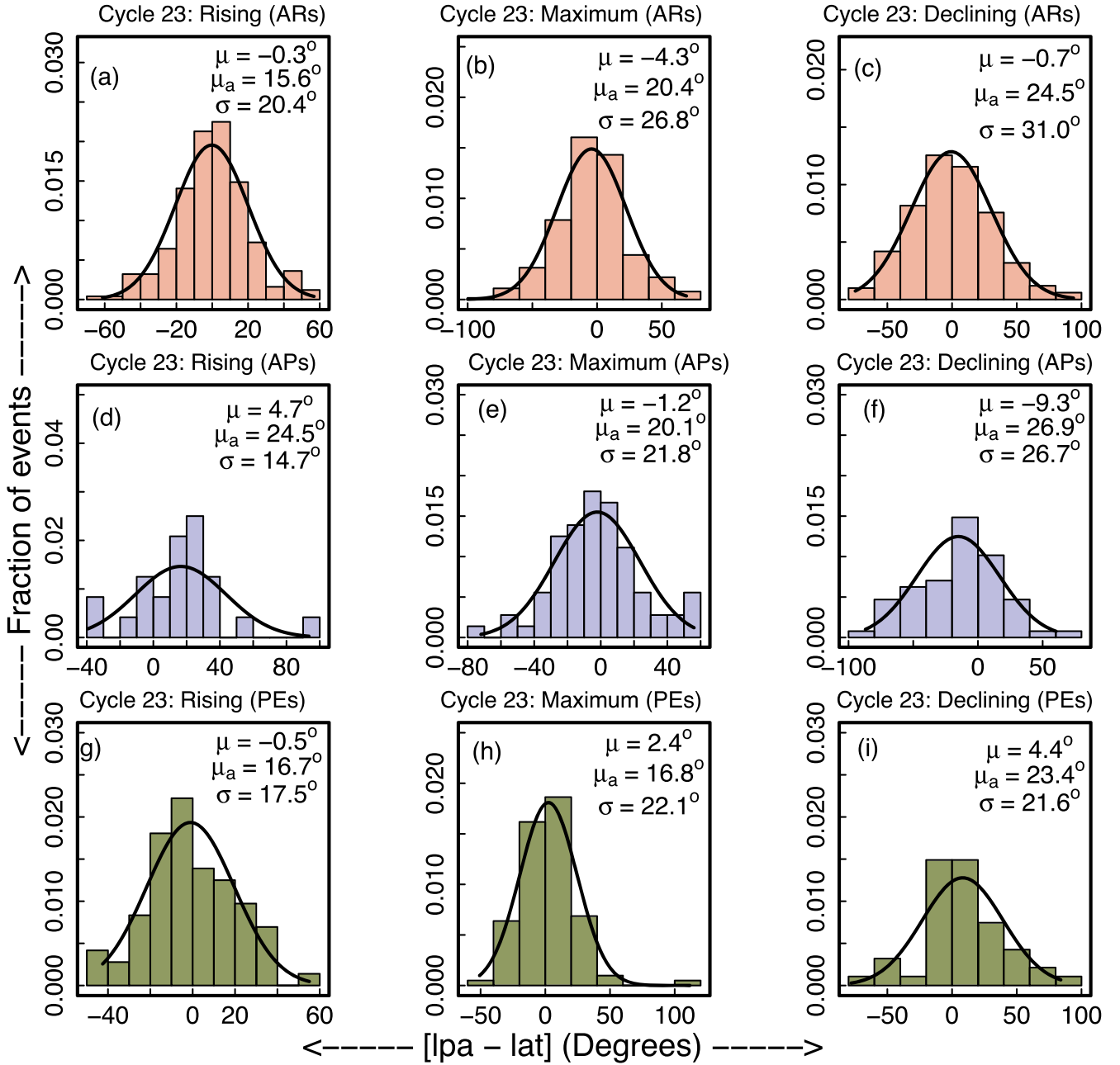


**Figure 13.** The distributions of the differences between the latitudes of the source regions of the CMEs and the position-angle equivalent latitudes of the CMEs, occurring during the rising, maximum, and declining phases of Cycle 23 (horizontally for each row), are plotted for CMEs originating from ARs, APs, and PEs (vertically for each column, corresponding to each phase of the solar cycle). A Gaussian is also fitted to each of the nine cases and the mean ( $\mu$ ), the absolute mean ( $\mu_a$ ), and the standard deviation ( $\sigma$ ) for each of the fitted Gaussians are also shown in each plot.

here, we plot in Figure 18 the longitude distributions for all CMEs in cycle 23 for the rising, maximum, and declining phases in panels (a), (b), and (c) and similarly for cycle 24 in panels (d), (e), and (f). We find that only during the rising phase in cycle 23 do we see a slight east–west asymmetry with a dominance from the western hemisphere, while the distributions of the longitudes during the other phases of cycles 23 and 24 do not show signatures of any distinct east–west asymmetry. Further, this small dominance may as well be attributed to some prolific AR that spuriously appeared in the western hemisphere and made the difference. Thus, an extension of this

study to a larger data set would be more insightful. However, it should be noted that Buss (1918) reported that there is a preferential contribution from the prominences on the eastern side of the Sun. Also, Hey & Hughes (1955) showed that there is an asymmetry in the longitudinal distribution of the flares associated with radio emission, and the dominance is toward the eastern side of the Sun. In Figure 17(c), we find our result in support of Buss (1918), as we also observe an eastward dominance, but again this figure is derived from position angles, and when we look into the distribution of the actual

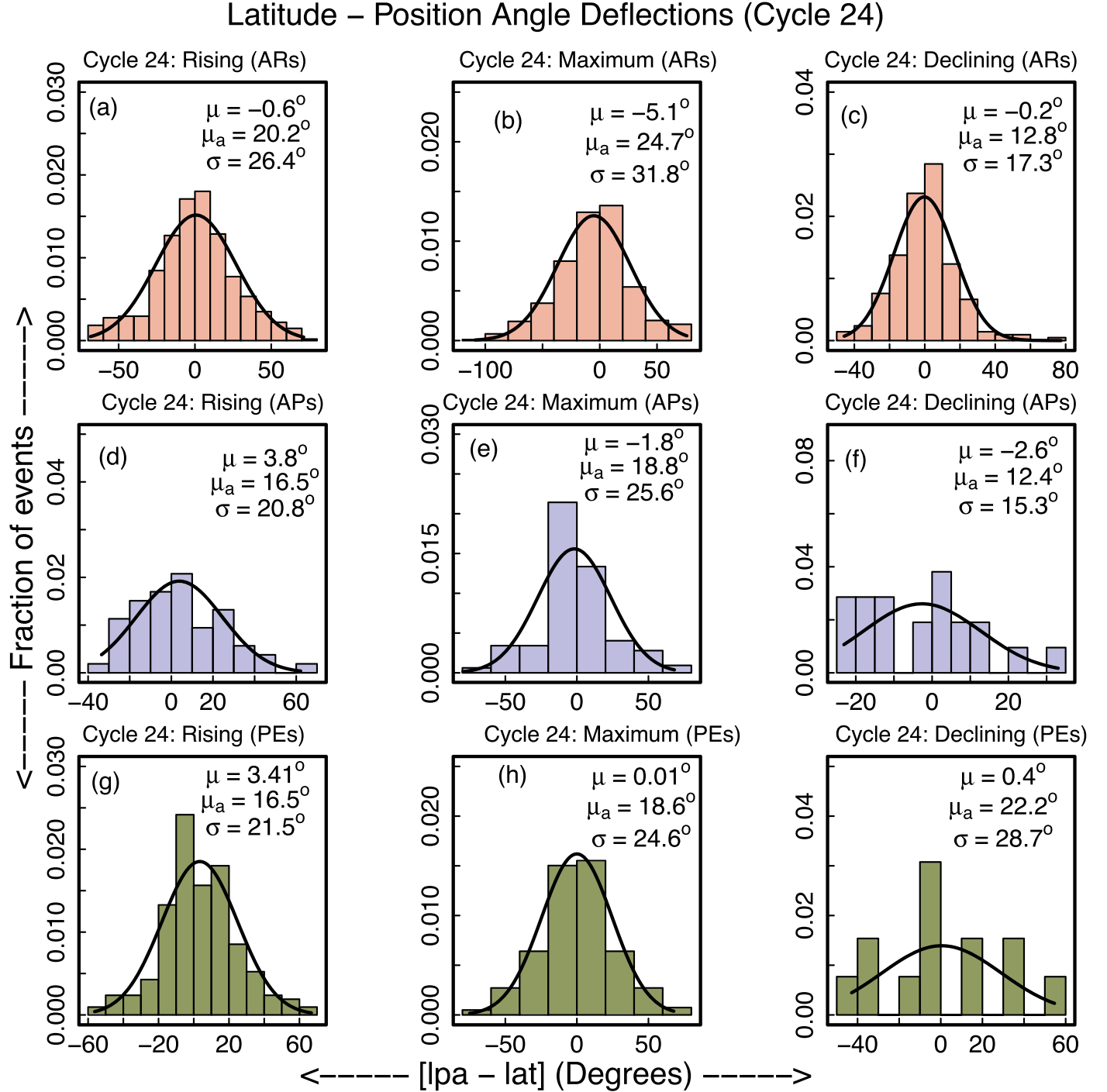


**Figure 14.** The distributions of the differences between the latitudes of the source regions of the CMEs and the position-angle equivalent latitudes of the CMEs, occurring during the rising, maximum, and declining phases of Cycle 24 (horizontally for each row), are plotted for the CMEs originating from ARs, APs, and PEs (vertically for each column, corresponding to each phase of the solar cycle). A Gaussian is also fitted to each of the nine cases and the mean ( $\mu$ ), the absolute mean ( $\mu_a$ ), and the standard deviation ( $\sigma$ ) for each of the fitted Gaussians are also shown in each plot.

longitudes in Figure 16(c), we no longer see the eastward dominance.

#### 4. Summary and Conclusions

A total of 3327 CMEs are selected from the CDAW catalog and have been studied in this work. The main aim of this work was to identify and associate each of them with the source region they are coming from, thereby cataloging the CMEs with their source regions, to help understand their properties

and the imprints of the source regions on the studied properties. After implementing certain constraints (rejecting the “very poor” CMEs, as quoted in the CDAW catalog) once the CMEs had been selected, the CMEs were segregated into slow ( $<300 \text{ km s}^{-1}$ ) and fast ( $>500 \text{ km s}^{-1}$ ) groups, based on the average linear speed as quoted in the CDAW catalog. Further, on the basis of certain spatial and temporal criteria, the CMEs were associated with the source regions they were coming from, thereby classifying the identified source regions into three

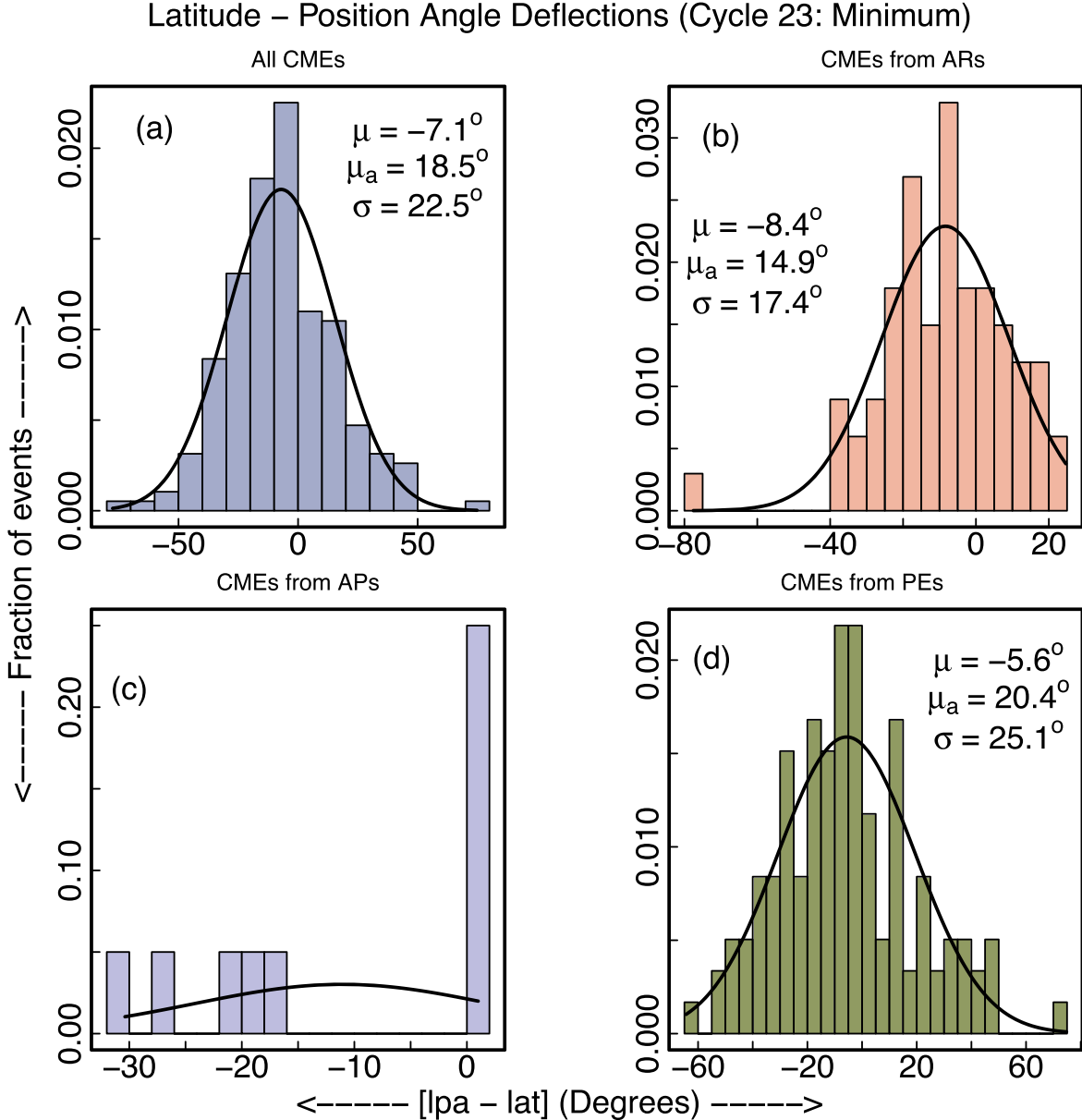


**Figure 15.** The distribution of the difference between the latitudes of the source regions of the CMEs, occurring during the minimum phase of Cycle 23, is plotted for all CMEs in panel (a) and for the ones originating from ARs, APs, and PEs in panels (b), (c), and (d), respectively. A Gaussian is also fitted to all four cases and the mean ( $\mu$ ), the absolute mean ( $\mu_a$ ), and the standard deviation ( $\sigma$ ) for each of the fitted Gaussians are also shown in each plot.

broad categories: (a) ARs; (b) APs; and (c) PEs. Although this study does not cover all the CMEs listed in the CDAW catalog (owing to the constraints mentioned in Section 2.2) for the past 25 yr of LASCO observations, we have tried to create an extensive database of CMEs with their source region properties, by considering CMEs that occurred during the different phases of cycle 23 and 24. In the following, we briefly list the main conclusions from this work:

1. A total of 3327 CMEs were studied, of which 1437 CMEs were identified as slow and 786 CMEs were identified as fast, while 1108 CMEs were identified as intermediate. The source regions of these CMEs were also identified, and it was found that 2037 CMEs came from ARs, 731 CMEs originated from PEs, and 369 CMEs came from APs (Figure 2).

2. The CMEs selected for this study were further subdivided into different categories (the rising phase, the maximum phase, and the declining phase), based on the phase of the solar cycle the CMEs occurred in. We found that the occurrences of slow and fast CMEs varied largely during these different phases of solar cycle (see Figure 3(a)). We found that as the cycle progresses from the rising phase to the maximum phase, the occurrences of slow CMEs decrease, while those of fast CMEs increase, which leads to almost similar occurrences of slow and fast CMEs during the cycle maximum. On the other hand, during the minimum, we find that the number of slow CMEs largely exceeds the number of fast CMEs.
3. The contributions of the different source regions also seem to be different during the different phases of the solar cycle (see Figure 3(b)). We found that the

**Table 3**  
The Mean, the Mean of the Absolute Deflections, and the Standard Deviation of the Gaussian Fitted to the Distribution of the Deflection Magnitude for the CMEs Coming from Different Source Regions during the Different Phases of Cycles 23 and 24

Distribution of Deflection Magnitude for	Mean Deflection ( $\mu$ )	Mean Absolute Deflection ( $\mu_a$ )	Standard Deviation ( $\sigma$ )
All CMEs	-1.5	19.9	26.3
CMEs from ARs	-2.1	20.4	26.9
CMEs from APs	-2.5	20.1	26.7
CMEs from PEs	0.8	18.2	23.9
CMEs from ARs (C23—Rising)	-0.3	15.6	20.4
CMEs from ARs (C23—Maximum)	-4.3	20.4	26.8
CMEs from ARs (C23—Declining)	-0.7	24.5	31.0
CMEs from APs (C23—Rising)	4.7	24.5	14.7
CMEs from APs (C23—Maximum)	-1.2	20.1	21.8
CMEs from APs (C23—Declining)	-9.3	26.9	26.7
CMEs from PEs (C23—Rising)	-0.5	16.7	17.5
CMEs from PEs (C23—Maximum)	2.4	16.8	22.1
CMEs from PEs (C23—Declining)	4.4	23.4	21.6
CMEs from ARs (C24—Rising)	-0.6	20.2	26.4
CMEs from ARs (C24—Maximum)	-5.1	24.7	31.8
CMEs from ARs (C24—Declining)	-0.2	12.8	17.3
CMEs from APs (C24—Rising)	3.8	16.5	20.8
CMEs from APs (C24—Maximum)	-1.8	18.8	25.6
CMEs from APs (C24—Declining)	-2.6	12.4	15.3
CMEs from PEs (C24—Rising)	3.41	16.5	21.5
CMEs from PEs (C24—Maximum)	0.01	18.6	24.6
CMEs from PEs (C24—Declining)	0.4	22.2	28.7
All CMEs (C23—Minimum)	-7.1	18.5	22.5
CMEs from ARs (C23—Minimum)	-8.4	14.9	17.4
CMEs from APs (C23—Minimum)	...	...	
CMEs from PEs (C23—Minimum)	-5.6	20.4	25.1

contribution of ARs dominated over the contributions from APs and PEs for most of the solar cycle, except during the minimum phase, during which the contribution from PEs tended to have a clear dominion over the other two.

4. The contributions of the different source regions to the slow and fast CMEs also varied during our study period. We found that for slow CMEs (Figure 4(a)), as the cycle progresses from the rising phase to the maximum, the contribution of CMEs from ARs increases, while during the minimum of cycle 23, we found the contribution of ARs to drop down, while the contribution from PEs increased. In the case of the fast CMEs (Figure 4(b)), we again found that the contribution of ARs dominated over the contributions from APs and PEs throughout the different phases of the solar cycle, although the relative contribution from the PEs also increased from the rising phase toward the maximum phase. We also found that the contribution of APs to fast CMEs was much higher than its contribution to the slow CMEs.
5. A distribution of the average linear speeds of the CMEs was studied and a power law (with a lower threshold  $v_{\min}$ ) was also fitted to the speed distribution (Figure 5), and we found different power laws for the speed distributions of CMEs from different source regions. The CMEs originating from PEs followed a much steeper power law, with a power-law index of -5.8, compared to the power laws in the cases of the CMEs from the ARs and APs (with power laws of -4.8 and -3.9, respectively). It should be noted that the estimated power-law index might be influenced by the choice of  $v_{\min}$ . Thus, in this work,

$v_{\min}$  is calculated by K-S distance minimization, and is not controlled manually, as manually constraining  $v_{\min}$  will introduce subjectivity bias into our analysis.

6. We plotted the distributions of the average speeds during different phases of cycle 23 and 24 (Figure 6), and found that the average speed in cycle 24 was less than the average speed in cycle 23, irrespective of the phase of the solar cycle under consideration. We also found that the speed distributions during the different phases in cycle 23 and 24 followed different power laws (Figure 6). The speed distributions in cycle 24 tended to follow a steeper power law than was the case for cycle 23, and this was independent of the phase of the cycle being compared. We also found the maximum phase to have the steepest power law in cycle 23 and the declining phase to have the steepest power law in cycle 24. In this context, it must be noted that since we are working with projected speeds, the estimated power laws will suffer from projection effects. However, from Figure 16, it is evident that most of the CMEs are originating from the limb of the Sun, and thus the projection-effect corrections would be minimal for most of the CMEs considered in this work.
7. We found strong imprints of the source regions on the power laws in the speed distributions in the different phases of cycles 23 and 24. In the rising phases of cycles 23 and 24 (Figure 7), we found the CMEs coming from PEs to follow much steeper power laws than the CMEs from ARs. This trend was also followed in the maximum phases of cycles 23 and 24 (Figure 8) and the minimum phase of cycle 23 as well (Figure 10), where the CMEs from PEs followed the steepest power laws. However,

## Distribution of Longitudes of Source Regions

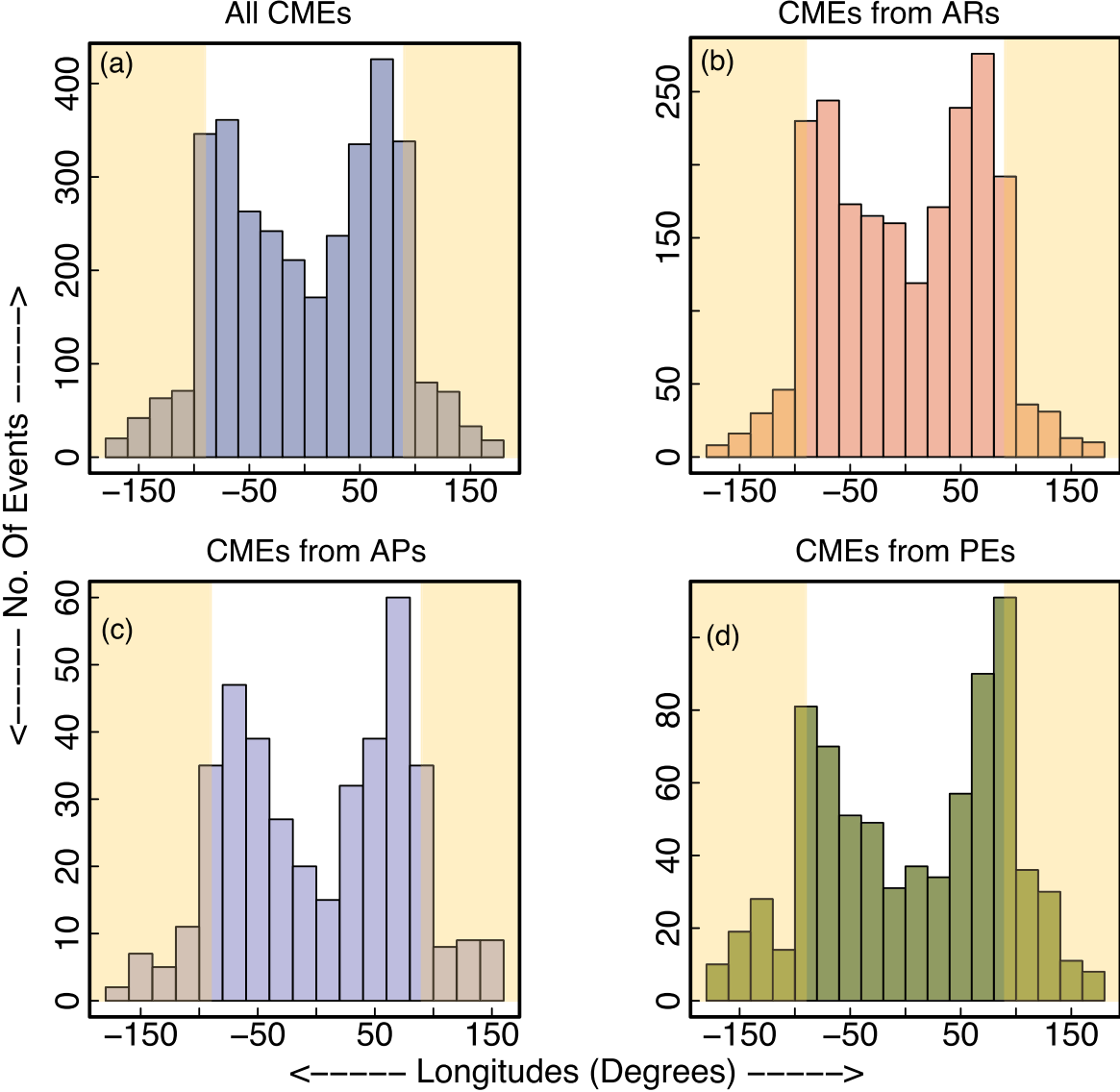


**Figure 16.** The distributions of the longitudes of the source regions are plotted for all CMEs in panel (a) and for the CMEs coming from ARs, APs, and PEs in panels (b), (c), and (d), respectively. The shaded regions in each plot highlight the importance of the STEREO mission in identifying and locating the source regions at the backside of the Sun (with respect to the Sun–Earth line).

during the declining phases of the cycles (Figure 9), we found the CMEs originating from ARs to follow the steepest power laws. It is crucial to note that in certain cases, a break in the tail of the distribution was noted, and to remove the influence of those data points on the fitted power law, an upper cutoff  $v_{\max}$  was also included. We found that although we found appreciable changes in the power laws in some cases, the overall trends and conclusions remained unchanged.

8. A study of the latitudinal deflections of the CMEs revealed the preferential equatorial deflection of the CMEs (Figure 11). It is important to note here that the mean deflection might be misleading, as deflection can be both positive as well as negative. Thus, quoting the mean of the absolute deflections will provide a better picture. By fitting Gaussians to the distributions of the magnitudes of deflection from different source regions, it was

found that the CMEs connected to ARs and APs tended to have wider spreads in deflection magnitude compared to the CMEs from PEs (Figure 12). However, during the minimum phase of cycle 23 (Figure 15), we found that the deflection magnitude had a higher standard deviation for the CMEs coming from PEs, as compared to the CMEs from ARs. We further found that in cycle 23 (Figure 13), the standard deviation in the distribution of the magnitude of deflection was at its minimum during the rising phase and at its maximum during the declining phase. This trend is independent of the source region from which the CMEs are originating. On the other hand, in cycle 24 (Figure 14), we found the standard deviation to be less in the declining phase and to be highest in the maximum phase. Thus, it seems that the trends of the deflections are different during the different phases of the

## Distribution of Position Angles of CMEs

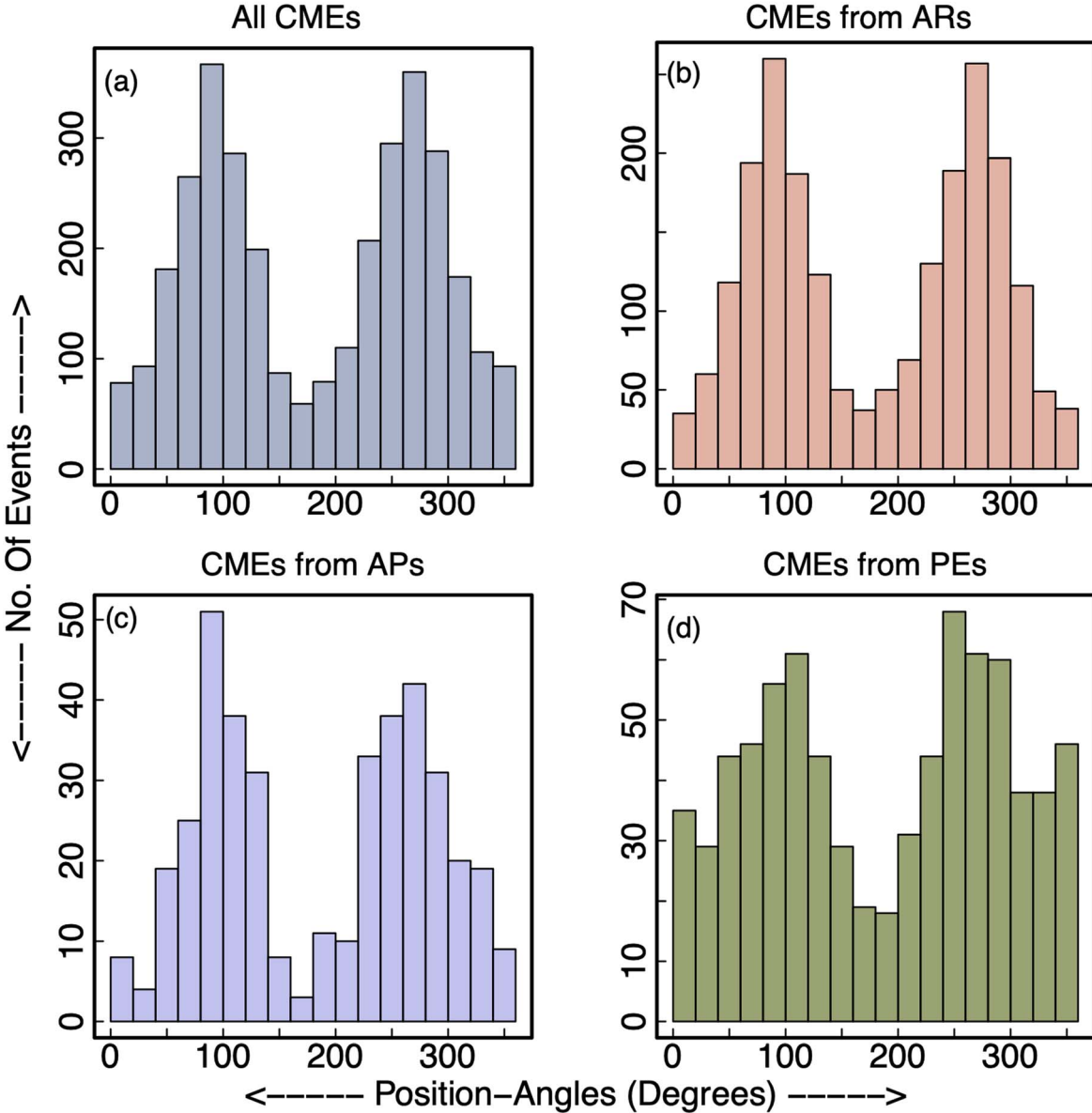


**Figure 17.** Distributions of the position angles of the CMEs are plotted for all CMEs in panel (a) and for the CMEs coming from ARs, APs, and PEs in panels (b), (c), and (d), respectively.

solar cycle, and they are also dependent on the solar cycle under consideration.

9. A study of the distribution of the longitudes of the source regions showed a double-peaked distribution, with an apparent east–west asymmetry, particularly in the rising phase of cycle 23, with a westward dominance (Figure 16). A plot of the distribution of the position angles of the CMEs, although they showed a similar bimodal distribution (Figure 17), nonetheless concealed the asymmetry in the distribution, as was evident from the distribution of the longitudes, thus indicating that drawing a conclusion based on the distribution of the position angles might not give the true picture and could be misleading. This apparent asymmetry could be a reflection of the fact that there is an abundance of limb CMEs, as CMEs originating around the central meridian

are generally less prone to being detected. Besides, the data set used in this study is taken from the CDAW catalog, which is based on observations taken along the Sun–Earth line. Also, analyzing the asymmetry based on the differences in height of the tallest columns might be misleading, as the observed differences in height of the tallest columns may have been contributed by some prolific ARs that may appear in one of the hemispheres, creating the difference. Thus, in the future, an extension of this study to an even larger data set, and to CMEs detected from multiple vantage points (Vourlidas et al. 2017) and based on unprojected quantities, will be important.

Thus, this CSR catalog, apart from providing a catalog of CMEs containing the source region information for a sample

## Distribution of Source Region Longitudes of all CMEs (Cycle 23 and 24)

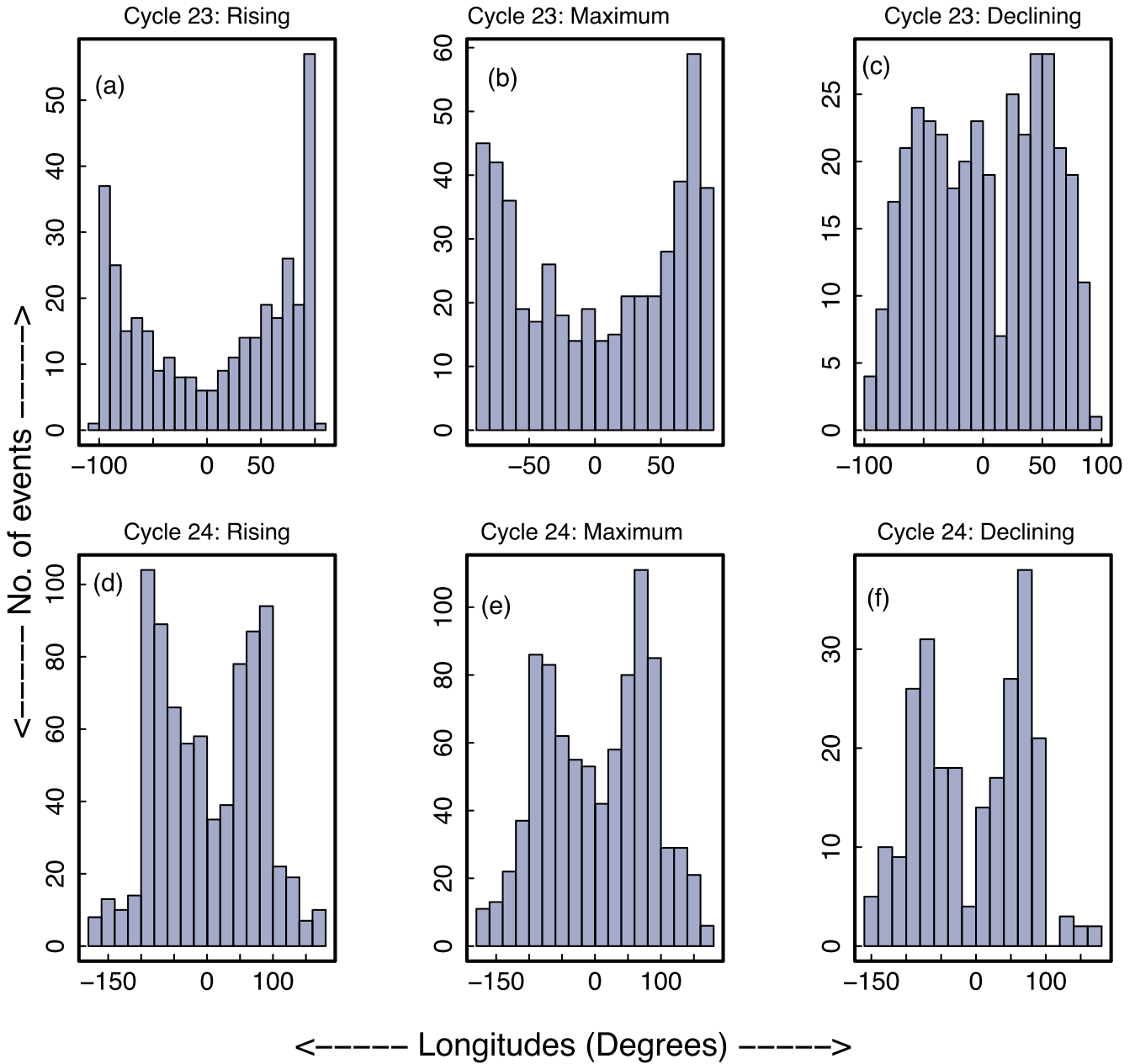


**Figure 18.** The distributions of the longitudes of all CMEs are plotted for the rising, maximum, and declining phases of cycle 23 in panels (a), (b), and (c), respectively, and similarly for cycle 24 in panels (d), (e), and (f).

set of 3327 CMEs, also encourages us to believe that our results provide evidence demonstrating that the source regions have strong imprints on several statistical properties of the CMEs. However, there are certain limiting aspects of this study, as discussed above, which mainly arise from the fact that the geometrical and kinematic parameters extracted from the CDAW catalog suffers from projection effects and from the fact that the CMEs were only recorded based on their detection along the Sun–Earth line. Another aspect worth noting is that not all CMEs occurring during the different phases of cycles 23 and 24 were included in this study, owing to the limitations discussed in Section 2.2. In the future, then, the results from this study could be further extended by considering all CMEs in the entire cycles of 23 and 24, using a multiple-vantage-point

CME catalog. Having said that, we also believe that these results will encourage future works to be dedicated to understanding the differences in the generation and propagation processes for CMEs coming from these different sources, as well as to exploring the significance of the contributions of statistical works on CME behaviors, thereby moving ourselves a further step closer toward more improved space weather predictions.

### Acknowledgments

We thank the anonymous reviewer for the careful and insightful comments that helped improve the manuscript. The SOHO/LASCO data used here are produced by a consortium

of the Naval Research Laboratory (USA), the Max-Planck-Institut für Aeronomie (Germany), the Laboratoire d’Astronomie (France), and the University of Birmingham (UK). SOHO is a project of international cooperation between ESA and NASA. We used the CDAW catalog data. This CME catalog is generated and maintained at the CDAW Data Center by NASA and The Catholic University of America in cooperation with the Naval Research Laboratory. The SECCHI data used here were produced by an international consortium of the Naval Research Laboratory (USA), the Lockheed Martin Solar and Astrophysics Lab (USA), the NASA Goddard Space Flight Center (USA), the Rutherford Appleton Laboratory (UK), the University of Birmingham (UK), the Max-Planck-Institut for Solar System Research (Germany), the Centre Spatial de Liège (Belgium), the Institut d’Optique Théorique et Appliquée (France), and the Institut d’Astrophysique Spatiale (France). We also acknowledge the SDO team for making the AIA data available. SDO is a mission for NASA’s Living With a Star (LWS) program. The authors acknowledge Kavya Bindu M for her contribution in preparing this catalog.

### ORCID iDs

Satabdwa Majumdar  <https://orcid.org/0000-0002-6553-3807>

Ritesh Patel  <https://orcid.org/0000-0001-8504-2725>

Vaibhav Pant  <https://orcid.org/0000-0002-6954-2276>

Dipankar Banerjee  <https://orcid.org/0000-0003-4653-6823>

### References

- Akiyama, S., Gopalswamy, N., Yashiro, S., & Michalek, G. 2019, AGUUFM , 2019, SH11D-3389
- Balmaceda, L. A., Vourlidas, A., Stenborg, G., & Dal Lago, A. 2018, *ApJ*, 863, 57
- Boursier, Y., Lamy, P., Llebaria, A., Goudail, F., & Robelus, S. 2009, *SoPh*, 257, 125
- Buss, A. A. 1918, *Natur*, 101, 5
- Byrne, J. P., Morgan, H., Habbal, S. R., & Gallagher, P. T. 2012, *ApJ*, 752, 145
- Clauset, A., Shalizi, C. R., & Newman, M. E. J. 2009, *SIAMR*, 51, 661
- Compagnino, A., Romano, P., & Zuccarello, F. 2017, *SoPh*, 292, 5
- Cremades, H., & Bothmer, V. 2004, *A&A*, 422, 307
- Delaboudinière, J. P., Artzner, G. E., Brnaud, J., et al. 1995, *SoPh*, 162, 291
- D’Huys, E., Berghmans, D., Seaton, D. B., & Poedts, S. 2016, *SoPh*, 291, 1561
- Domingo, V., Fleck, B., & Poland, A. I. 1995, *SoPh*, 162, 1
- Gao, P.-X., Li, T., & Zhang, J. 2014, *RAA*, 14, 1289
- Gilbert, H. R., Holzer, T. E., Burkepile, J. T., & Hundhausen, A. J. 2000, *ApJ*, 537, 503
- Gopalswamy, N., Akiyama, S., Yashiro, S., et al. 2014, *GeoRL*, 41, 2673
- Gopalswamy, N., Akiyama, S., Yashiro, S., et al. 2020, *JPhCS*, 1620, 012005
- Gopalswamy, N., Shimojo, M., Lu, W., et al. 2003, *ApJ*, 586, 562
- Gopalswamy, N., Yashiro, S., Mäkelä, P., et al. 2018, *ApJL*, 863, L39
- Gopalswamy, N., Yashiro, S., Michalek, G., et al. 2009, *EM&P*, 104, 295
- Gosling, J. T. 1993, *JGR*, 98, 18937
- Gui, B., Shen, C., Wang, Y., et al. 2011, *SoPh*, 271, 111
- Hathaway, D. H. 2015, *LRSP*, 12, 4
- Hey, J. S., & Hughes, V. A. 1955, *MNRAS*, 115, 605
- Howard, R. A., Moses, J. D., Vourlidas, A., et al. 2008, *SSRV*, 136, 67
- Hundhausen, A. J., Sawyer, C. B., House, L., Illing, R. M. E., & Wagner, W. J. 1984, *JGR*, 89, 2639
- Jha, B. K., Hegde, M., Priyadarshi, A., et al. 2022, *FrASS*, 9, 1019751
- Kaiser, M. L., Kucera, T. A., Davila, J. M., et al. 2008, *SSRV*, 136, 5
- Kim, R. S., Park, S. H., Jang, S., Cho, K. S., & Lee, B. S. 2017, *SoPh*, 292, 66
- Lamy, P. L., Floyd, O., Boclet, B., et al. 2019, *SSRV*, 215, 39
- Lara, A. 2008, *ApJ*, 688, 647
- Lemen, J., Title, A., Boerner, P., et al. 2011, *SoPh*, 275, 17
- Lugaz, N., Farrugia, C. J., Winslow, R. M., et al. 2017, *ApJ*, 848, 75
- Lyot, B. 1930, *CRAS*, 191, 834
- Majumdar, S., Pant, V., Patel, R., & Banerjee, D. 2020, *ApJ*, 899, 6
- Majumdar, S., Patel, R., & Pant, V. 2022, *ApJ*, 929, 11
- Majumdar, S., Patel, R., Pant, V., & Banerjee, D. 2021a, *ApJ*, 919, 115
- Majumdar, S., Tadepalli, S. P., Maity, S. S., et al. 2021b, *SoPh*, 296, 62
- Moore, R. L., Sterling, A. C., & Suess, S. T. 2007, *ApJ*, 668, 1221
- Morgan, H., Byrne, J. P., & Habbal, S. R. 2012, *ApJ*, 752, 144
- Muller, D., Fleck, B., Dimitoglou, G., et al. 2009, *CSE*, 11, 38
- Müller, D., Nicula, B., Felix, S., et al. 2017, *A&A*, 606, A10
- Olmedo, O., Zhang, J., Wechsler, H., Poland, A., & Borne, K. 2008, *SoPh*, 248, 485
- Pant, V., Majumdar, S., Patel, R., et al. 2021, *FrASS*, 8, 73
- Pant, V., Willems, S., Rodriguez, L., et al. 2016, *ApJ*, 833, 80
- Robbrecht, E., & Berghmans, D. 2004, *A&A*, 425, 1097
- Ruzmaikin, A., Feynman, J., & Stoev, S. A. 2011, *JGRA*, 116, A04220
- Schwenn, R. 2006, *LRSP*, 3, 2
- Schwenn, R., dal Lago, A., Huttunen, E., & Gonzalez, W. D. 2005, *AnGeo*, 23, 1033
- Skirgiello, M. 2005, *AnGeo*, 23, 3139
- Subramanian, P., & Dere, K. P. 2001, *ApJ*, 561, 372
- Tripathi, D., Bothmer, V., & Cremades, H. 2004, *A&A*, 422, 337
- Vourlidas, A., Balmaceda, L. A., Stenborg, G., & Dal Lago, A. 2017, *ApJ*, 838, 141
- Vourlidas, A., Balmaceda, L. A., Stenborg, G., & Lago, A. D. 2017, *ApJ*, 838, 141
- Wang, Y., Chen, C., Gui, B., et al. 2011, *JGRA*, 116, A04104
- Wang, Y.-M., & Colaninno, R. 2014, *ApJL*, 784, L27
- Webb, D., & Howard, T. 2012, *LRSP*, 9, 3
- Webb, D. F., & Hundhausen, A. J. 1987, *SoPh*, 108, 383
- White, E. P., Enquist, B. J., & Green, J. L. 2008, *Ecology*, 89, 905
- Wuelser, J.-P., Lemen, J. R., Tarbell, T. D., et al. 2004, *Proc. SPIE*, 5171, 111
- Yashiro, S., & Gopalswamy, N. 2009, in IAU Symp. 257, Universal Helophysical Processes, ed. N. Gopalswamy & D. F. Webb (Cambridge: Cambridge Univ. Press), 233
- Zhou, G., Wang, J., & Cao, Z. 2003, *A&A*, 397, 1057